

MACROPHAGES

A common framework of monocyte-derived macrophage activation

David E. Sanin^{1,2*}, Yan Ge³, Emilija Marinkovic³, Agnieszka M. Kabat^{1,2}, Angela Castoldi¹, George Caputa¹, Katarzyna M. Grzes^{1,2}, Jonathan D. Curtis², Elizabeth A. Thompson², Sebastian Willenborg⁴, Stefanie Dichtl⁵, Susanne Reinhardt⁶, Andreas Dahl⁶, Erika L. Pearce^{1,2,7*}, Sabine A. Eming^{4,8,9,10*}, Alexander Gerbaulet^{3*}, Axel Roers^{3*}, Peter J. Murray^{5*}, Edward J. Pearce^{1,2,11,12*†}

Copyright © 2022
The Authors, some
rights reserved;
exclusive licensee
American Association
for the Advancement
of Science. No claim
to original U.S.
Government Works

Macrophages populate every organ during homeostasis and disease, displaying features of tissue imprinting and heterogeneous activation. The disconnected picture of macrophage biology that has emerged from these observations is a barrier for integration across models or with in vitro macrophage activation paradigms. We set out to contextualize macrophage heterogeneity across mouse tissues and inflammatory conditions, specifically aiming to define a common framework of macrophage activation. We built a predictive model with which we mapped the activation of macrophages across 12 tissues and 25 biological conditions, finding a notable commonality and finite number of transcriptional profiles, in particular among infiltrating macrophages, which we modeled as defined stages along four conserved activation paths. These activation paths include a “phagocytic” regulatory path, an “inflammatory” cytokine-producing path, an “oxidative stress” antimicrobial path, or a “remodeling” extracellular matrix deposition path. We verified this model with adoptive cell transfer experiments and identified transient RELM α expression as a feature of monocyte-derived macrophage tissue engraftment. We propose that this integrative approach of macrophage classification allows the establishment of a common predictive framework of monocyte-derived macrophage activation in inflammation and homeostasis.

INTRODUCTION

Macrophages can be found in every organ displaying distinct transcriptional profiles (1, 2) and specializing to their tissue of residence during homeostasis (3). Macrophage tissue engraftment occurs early during embryonic development (4, 5), with site-specific contributions from circulating monocytes to the replenishment of tissue-resident pools (5–9). The extent to which tissue macrophages are replenished by monocytes during adulthood is an area of debate with ongoing revisions of macrophage ontogeny models (4, 6, 10) only recently expanding to humans (11). Because focus has shifted to the origin of macrophages and the impact of tissue imprinting (1), the engagement of recruited versus resident macrophages during the immune response has received greater scrutiny. However, these

efforts have been hampered by the limitations inherent to phenotyping techniques that rely on bulk population averaging (e.g., RNA sequencing), few simultaneous measurements (e.g., flow cytometry), and poorly characterized macrophage subset markers. This is especially challenging because incoming monocytes are able, with time, to adopt nearly indistinguishable transcriptional profiles to resident macrophages in the tissue that they enter (12). Despite these limitations, some have suggested that macrophages in different tissues should be regarded as entirely different cells (3) or that paradigms of macrophage M1 (classical)/M2 (alternative) activation should be abandoned (13–15). This latter view in particular is supported by the extensive plasticity that macrophages display when stimulated with cocktails of cytokines, pattern recognition receptor ligands, and other immunomodulatory molecules (16, 17). Thus, the emerging picture of macrophage activation suggests a flexible spectrum of different activation states, with tissue- and context-specific parameters viewed as dominant predictors of macrophage function.

This complex landscape of macrophage phenotype has been further advanced by the emergence of single-cell RNA sequencing (scRNA-seq), which overcomes the limitations of bulk population averaging and does not rely on previously defined surface markers for macrophage subset sorting. As more studies using this technique are published, the observed heterogeneity in macrophage activation states has further increased, with previously unidentified subsets or phenotypes frequently identified (18–27). Consequently, macrophage biology currently lacks a common framework to describe the state of activation of macrophages in tissues.

In light of this evolving situation, we asked whether the construction of such a common framework would be possible, reasoning that a unifying model could be built by comparing macrophage activation profiles across tissues under multiple inflammatory conditions. We expected that either we would succeed in finding common

¹Department of Immunometabolism, Max Planck Institute of Immunobiology and Epigenetics, 79108 Freiburg, Germany. ²Department of Oncology, Bloomberg-Kimmel Institute for Cancer Immunotherapy, Johns Hopkins University School of Medicine, Baltimore, MD 21287, USA. ³Institute for Immunology, Medical Faculty Carl Gustav Carus, TU Dresden, Fetscherstr. 74, 01307 Dresden, Germany. ⁴Department of Dermatology, University of Cologne, Kerpenerstr. 62, 50937 Cologne, Germany. ⁵Max Planck Institute of Biochemistry, 82152 Martinsried, Germany. ⁶DRESDEN-concept Genome Center, TU Dresden, Fetscherstr. 105, 01307 Dresden, Germany. ⁷Department of Biochemistry and Molecular Biology, Johns Hopkins University Bloomberg School of Public Health, Baltimore, MD 21287, USA. ⁸Center for Molecular Medicine Cologne (CMMC), University of Cologne, Cologne, Germany. ⁹Cologne Excellence Cluster on Cellular Stress Responses in Aging-Associated Diseases (CECAD), University of Cologne, Cologne, Germany. ¹⁰Institute of Zoology, Developmental Biology Unit, University of Cologne, Cologne, Germany. ¹¹Faculty of Biology, University of Freiburg, 79104 Freiburg, Germany. ¹²Department of Molecular Microbiology and Immunology, Johns Hopkins University Bloomberg School of Public Health, Baltimore, MD 21287, USA.

*Corresponding author. Email: epearce7@jhmi.edu (E.J.P.); david.sanin@jhu.edu (D.E.S.); epearce6@jhmi.edu (E.L.P.); sabine.eming@uni-koeln.de (S.A.E.); alexg@msx.tu-dresden.de (A.G.); axel.roers@tu-dresden.de (A.R.); murray@biochem.mpg.de (P.J.M.)

†Lead contact.

activation features or that tissue-specific transcriptional programs would dominate the data. Accordingly, we built a predictive model with which we mapped the activation of macrophages across 12 mouse tissues and 25 biological conditions, finding a common and finite number of transcriptional profiles which we modeled as stages along four conserved activation paths. These activation stages placed cells with varying frequencies along a “phagocytic” regulatory path, an “inflammatory” cytokine-producing path, an “oxidative stress” antimicrobial path, or a “remodeling” extracellular matrix (ECM) deposition path. We verified our model with adoptive cell transfer experiments, noting that incoming monocytes adopt all the transcriptional signatures that we detected. Moreover, we identified transient resistin-like molecule alpha (RELMA) expression as a feature of macrophage tissue engraftment and propose that historical RELMA expression may serve to identify monocyte contribution to tissue-resident macrophage populations. Last, we propose that this integrative approach of macrophage classification allows the establishment of a common predictive framework of monocyte-derived macrophage activation (<https://t.jh.edu/macrophage-framework>) that may serve to contextualize these cells in future studies and, for this reason, we provide a validated list of surface markers that may be used to identify these cells.

RESULTS

Macrophages in inflammatory conditions coexist in diverse functional states

We aimed to contextualize macrophage heterogeneity across tissues in diverse inflammatory conditions, specifically defining common aspects of macrophage activation during infection and inflammation (Fig. 1A). For this purpose, we built a reference dataset (Fig. 1, A and B) based on two inflammatory conditions representing either a classical inflammatory response during bacterial infection using *Listeria monocytogenes* (*L. mono*) or a type 2 immune response during *Heligmosomoides polygyrus* (*H. poly*) helminth infection (fig. S1). We reasoned that these settings, which induce multicellular and systemic responses, provide a broad spectrum of macrophage activation improving the completeness of our reference dataset. We performed scRNA-seq on all stromal vascular fraction cells from mesenteric fat (fig. S2A), adjacent to the site of *H. poly* infection, and popliteal fat (fig. S2B), which is directly invaded by *L. mono* after footpad injection. We observed a rich infiltration of CD45⁺ cells expressing archetypical cytokines associated with type 2 and type 1 immunity (fig. S1). We then examined macrophage gene expression markers in these datasets (fig. S2, A and B) and extracted, balanced (500 cells per condition), integrated, and reclustered identified macrophages. Gene expression was distinct within each resulting cluster (fig. S2C and data file S1) and associated with specific biological processes (Fig. 1C and table S1).

We observed that clusters 0 and 3 were enriched for genes associated with macrophage alternative activation (e.g., *Cd36*, *Clec10a*, and *Mrc1*), antigen presentation (e.g., *H2-Aa*, *H2-Eb1*, and *H2-Ab1*), and the complement cascade (e.g., *C1qc* and *C1qb*) (Fig. 1C, fig. S2C, and data file S1). Cluster 2 was enriched for genes involved in ECM-receptor interactions (e.g., *Cd44*, *Sdc1*, and *Fn1*) and cytoskeleton regulation (e.g., *Pfn1*, *Actg1*, and *Tmsb4x*). Cluster 4 displayed high expression of genes participating in antigen presentation (e.g., *H2-Oa*, *H2-DMb2*, and *Cd74*). Clusters 5, 6, and 7 were enriched for genes associated with the phagosome (e.g., *Fcgr1*, *Ncf4*,

and *Fcgr3*) and oxidative stress (e.g., *Prdx5*, *Txn1*, and *Gsr*), with cluster 6 in particular enriched for innate immune response genes (e.g., *Ifitm3*, *Fcgr1*, and *Isg20*). ECM organization genes (e.g., *Col1a1*, *Col3a1*, and *Ddr2*) were highest in cluster 8, whereas cluster 9 displayed high expression of cell cycle-associated genes (e.g., *Cks1b*, *H2afx*, and *Cks2*). Cluster 1, which occupied the center of the Uniform Manifold Approximation and Projection (UMAP), had no distinctly regulated genes (fig. S2C and data file S1) and therefore no pathway assignment (Fig. 1C). Thus, our analysis shows that macrophages within a tissue simultaneously specialize into multiple functional categories, corroborating findings in other studies where this diversity has been reported (21, 23, 26).

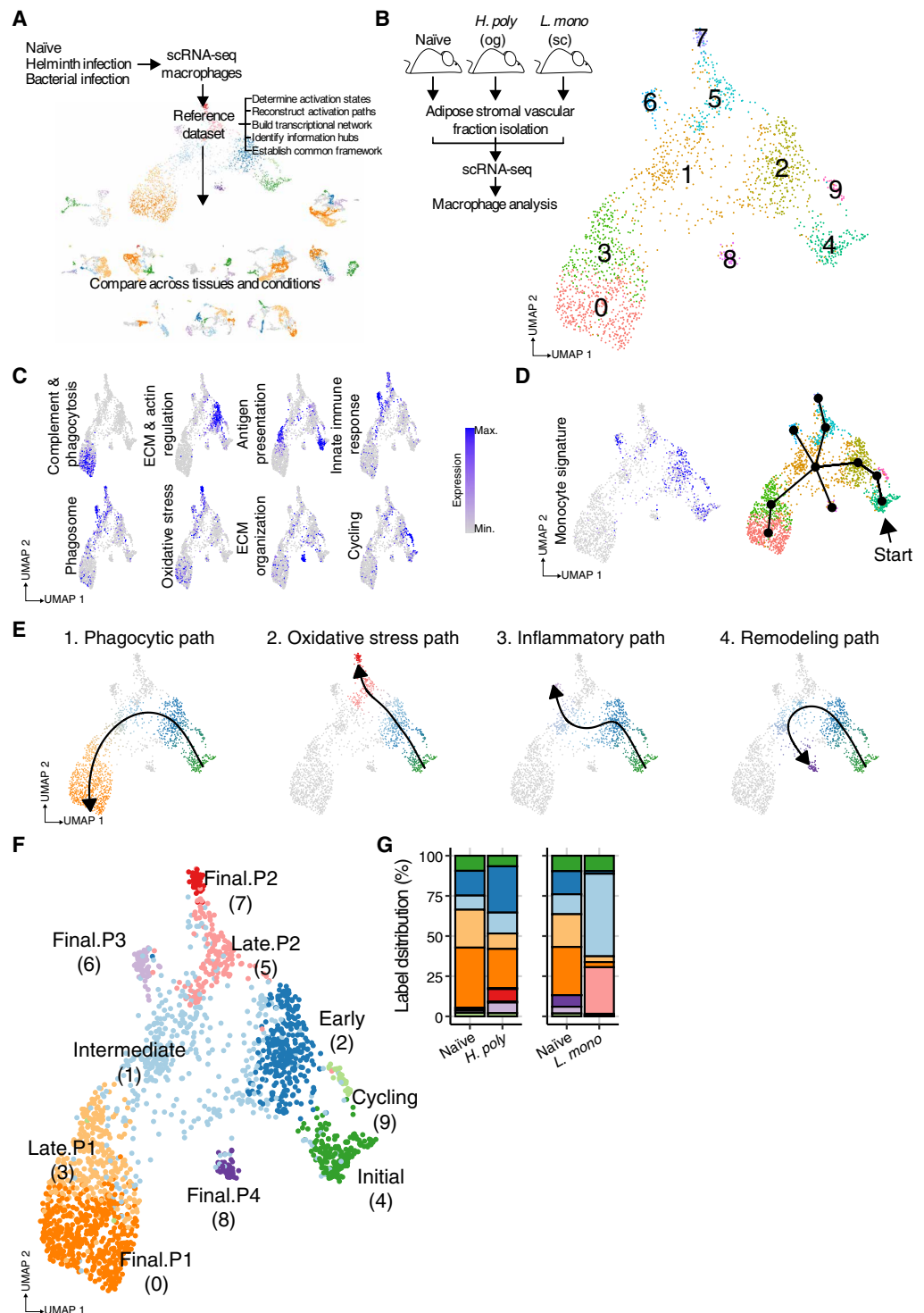
Macrophages in inflammatory conditions are arranged along activation paths

Cluster 1 could not be associated with a distinct function as it displayed no up-regulated genes using the thresholds that we established (average log fold change > 1, percent cells expressing gene > 0.4, and an adjusted $P < 0.01$). We reasoned that cluster 1 could represent an intermediate state of activation, suggesting that rather than different populations of macrophages, our analysis captured activation paths being followed by infiltrating monocyte-derived macrophages. To test this hypothesis, we used Slingshot (28) to generate a model of macrophage activation in the tissue (Fig. 1, D and E). To establish a starting point for this analysis, we calculated a monocyte gene set score (Fig. 1D and table S1) (1) and then selected cluster 4 (Fig. 1, B to D, black arrow), as it displayed a monocyte signature as well as increased major histocompatibility complex class II (MHC-II) expression, in line with reported monocyte-to-macrophage transitions (29).

Our analysis identified four activation paths that we labeled as phagocytic, oxidative stress, inflammatory, and remodeling according to the enriched pathway at the end point clusters of each lineage (Fig. 1E). Our analysis also revealed three common stages of macrophage activation, which we named according to their relative position in the pseudotime progression as initial-, early-, and intermediate-stage (clusters 4, 2, and 1, respectively). The remaining clusters were renamed as either late.P#- or final.P#-stage (Fig. 1F); for example, late.P1-stage corresponded to cells in the cluster in activation path 1 (P1) that is between the intermediate and final stage. We complemented our approach with two alternative strategies of data integration, specifically the Seurat (30) implementation of Harmony (fig. S2D) (31) and the scanpy (32) implementation of batch balanced k-nearest neighbors (BBKNN) (33) followed by a partition-based graph abstraction (PAGA) (34) to infer activation trajectories (fig. S2E). Both approaches broadly recapitulated our initial results. Initial-stage cells were closely connected to those in early-stage, which then transitioned through intermediate-stage that split into cells in the phagocytic (P1), inflammatory (P3), and remodeling (P4) paths. Our clustering and labeling results were not greatly altered by alternative data processing approaches (fig. S2, D and E), with the overall conservation of global structure and relationship between the proposed stages supporting further exploration.

Next, we investigated how these activation stages were distributed across biological conditions (Fig. 1G). We observed that the distribution in macrophages from naïve mice into different functional stages in different fat deposits was comparable, and diverse, perhaps indicating an active process of macrophage activation as monocytes replenish these sites in steady state (Fig. 1G). We noted that *L. mono*

Fig. 1. Macrophage activation in inflamed tissues follows predefined paths. (A) Schematic depiction of reference dataset construction, outlining overall goals of strategy. (B) scRNA-seq analysis of macrophages (cells = 2000) from the stromal vascular fraction of adipose tissue from naïve, *H. poly*-, or *L. mono*-infected animals ($n = 1$ to 8 per group) shown as a UMAP, highlighting identified clusters. og, oral gavage; sc, subcutaneous. (C) Relative levels (low, gray; high, blue) of gene set scores associated with identified clusters. (D) Relative levels (low, gray; high, blue) of gene set scores associated with monocyte signature (left) and predicted lineage breaking points (right). (E) Lineage and pseudotime calculation showing activation trajectories. Cells assigned to identified paths are colored to match stage labels. Nonparticipating cells are shown in gray. (F) UMAP labeled according to path progression indicating shared (initial > early > intermediate) and path specific (phagocytic: late.P1 > final.P1; oxidative stress: late.P2 > final.P2; inflammatory: final.P3; remodeling: final.P4) macrophage activation stages. Cluster number indicated in brackets. (G) Activation stage distribution shown as a percentage of total cells per biological condition.



infection favored the oxidative stress path, whereas *H. poly* infection favored the phagocytic path when compared with each other (Fig. 1G). However, all activation stages were present in each condition, underscoring the limitations of bulk phenotyping to capture macrophage activation ex vivo. Moreover, the changes in diversity induced by infection were notably different between the inflammatory conditions studied. Whereas *H. poly* infection resulted in increases in numbers of cells within less well-represented activation stages, *L. mono* infection resulted in two activation stages becoming dominant. These differences could be explained not only by the specific immune responses tailored to the pathogens involved but also by the time at which samples were collected [table S2; day 1 p.i. (post-infection), for the *L. mono* dataset, day 14 p.i. for the *H. poly* dataset].

In summary, our model predicts that macrophages in an inflamed tissue progress through activation stages with distinct transcriptional profiles and that the balance of this progression is influenced by the type of immune response that dominates the microenvironment. Last, our model suggests that tissue can become dominated by relatively few activation stages, yet macrophages committed to multiple paths coexist.

Macrophages transition through a RELMa-expressing activation stage

We complemented our differential gene expression analysis (fig. S2C) by modeling gene expression as a function of pseudotime (Fig. 2A), reasoning that transcript levels would be regulated as macrophages progress along activation paths (Fig. 1, E and F). We included in this analysis only the top 2000 most variable genes in the cells of each path and ranked the resulting models on the basis of the *P* value of the association of pseudotime and gene expression (fig. S3A). We found that collectively, the expression of 828 genes ($P < 1 \times 10^9$) could be modeled in this way, and we show the top most significant association for each pathway (Fig. 2B). We observed that the regulation of typical macrophage activation markers corresponded to defined activation paths (Fig. 2C and fig. S3B). For instance, cells in the phagocytic path exhibited a steep and continuous increase in the alternative activation marker *Mrc1* and the mitochondrial metabolism gene *mt-Co1* as a function of pseudotime (Fig. 2C). Conversely, expression of inflammatory *Il1b* was only retained at high levels in the inflammatory and remodeling paths (Fig. 2C).

Exploring the relationship between RELMa encoding gene *Retnla* and pseudotime, we observed that our model predicted a wave of expression early during activation (Fig. 2D). Our data revealed that *Retnla* was expressed not only in cells committed to the phagocytic path (P1) (Fig. 2D), which also expressed other markers of alternative macrophage activation (Fig. 2C and data file S1), but also in early-stage cells shared by all paths (Fig. 2D). Moreover, we identified *Retnla* and *Ear2* coexpression as unique to early-stage cells (Fig. 2D). We reasoned that if our model was correct, then monocytes would express *Retnla* shortly after entering a tissue regardless of the inflammatory condition. To test this, we isolated bone marrow monocytes from CD45.1⁺ mice (fig. S3C) and adoptively transferred them into the peritoneal cavity of CD45.2⁺ naïve hosts (Fig. 2E). We evaluated the abundance of *Retnla* mRNA and RELMa protein in CD45.1⁺ macrophages recovered 2, 4, and 8 days after adoptive transfer (Fig. 2F and fig. S3D). Confirming our predictions, monocyte-derived macrophages expressed RELMa 4 days after adoptive transfer, and ~80% of the cells were positive for this molecule after 8 days (Fig. 2F). RELMa induction occurred in the absence of interleukin-4 receptor alpha (IL-4Rα) signaling, as we did not detect changes in RELMa expression in host tissue-resident macrophages in the peritoneal cavity and IL-4Rα^{-/-} monocytes displayed similar RELMa expression compared with IL-4Rα^{+/+} cells (Fig. 2G). Last, mature CD45.1⁺ peritoneal macrophages did not express RELMa after transfer into CD45.2⁺ naïve recipients (Fig. 2G). Thus, our experimental data support the view that monocytes differentiating into macrophages early after entry into a tissue begin to express RELMa independently of IL-4 signaling.

Macrophage-specific RELMa deficiency leads to poor monocyte/macrophage infiltration of the lung in a model of fibrosis (35), which suggests that RELMa might be required for macrophage tissue engraftment. To test this, we isolated monocytes from the bone marrow of RELMa^{-/-} animals (36) and then adoptively transferred them into the peritoneal cavity of CD45.1⁺ hosts and evaluated their ability to engraft compared with wild-type (WT) macrophages (Fig. 2H). We recovered fewer RELMa^{-/-} cells 8 days after transfer (Fig. 2H). Furthermore, the proportion of CD115⁺F4/80⁺ macrophages was significantly reduced in RELMa^{-/-} versus WT controls. These results indicate that RELMa serves as a marker of macrophage tissue engraftment and may also function to maintain the identity

of the infiltrating cells, because CD115 (CSF1R) is a critical macrophage growth factor receptor. These findings support our predicted model of macrophage activation and explain evidence of historical *Retnla* expression in tissue-resident macrophages (37). Moreover, RELMa expression has been used to identify cells of a distinct tissue-restricted phenotype (21) or in an immature state of differentiation (8). Our data are broadly in agreement with these past reports and indicate that historical RELMa expression should be evident in tissues where circulating monocytes replace tissue-resident macrophages. Moreover, our data suggest that transit via a RELMa⁺ stage is a common feature of all macrophages and not restricted to a single tissue or macrophage subset.

Macrophage activation stages are conserved across tissues and inflammatory conditions

Our findings in the adipose tissue datasets indicate that observed heterogeneity in macrophage activation can be accounted for by macrophages transiting through defined activation paths after they enter a tissue. To evaluate these ideas further, we used our adipose tissue dataset as a reference to interrogate multiple other situations of tissue inflammation (table S2). We took advantage of a recent data transfer implementation that enables the construction of large cell atlases (38), assigning probability-scored labels and performing data imputation (i.e., inferring and assigning missing gene expression values). This strategy is highly accurate for label transfer from a reference dataset (39) yet can overcorrect batch effects while sacrificing biological variability (40). We tested this approach on datasets that contained a mixture of macrophages and other CD45⁺ cells, using the adipose tissue as a reference and extensively optimizing label transfer/imputation parameters, reasoning that only macrophages should have high probability scores resulting from transfer of activation stage labels (fig. S4, A to H). Using a probability threshold of 80% (or 0.8), almost exclusively macrophages were assigned an activation stage label in datasets with abundant (fig. S4, A to D) and scarce macrophage populations (fig. S4, E to H). Thus, we proceeded to interrogate multiple tissues and inflammatory conditions using this approach.

We retrieved publicly available scRNA-seq datasets spanning nine tissues and 13 inflammatory conditions plus healthy controls, including infections, injuries, cancer, and dietary interventions (Fig. 3 and table S2). We retained only macrophages by filtering cells based on established markers (table S1), harmonized the data within each tissue to remove batch effects, and applied the transfer process, assigning cells to a previously defined activation stage, with a label probability (Fig. 3) and imputed gene expression data (fig. S4, I to Q). Imputed data were used to cluster and calculate a UMAP for each dataset (fig. S5). Where a single label dominated a cluster, and a portion of the cells within the cluster had a high-label probability score, the corresponding label was assigned to the entire cluster (e.g., fig. S5B, clusters 3, 4, 6, and 7). Macrophages that did not meet these criteria were marked as “not classified.” We identified most of the activation stages defined in our reference with a reasonable proportion of cells with a high-label transfer probability in all interrogated datasets (Fig. 3).

The distribution of activation stage labels was different in each studied tissue and then modified by the corresponding inflammatory condition (Fig. 3). This could reflect the influence of the tissue microenvironment in shaping the immune response, as well as the way in which the immune response is tailored to a specific insult. For

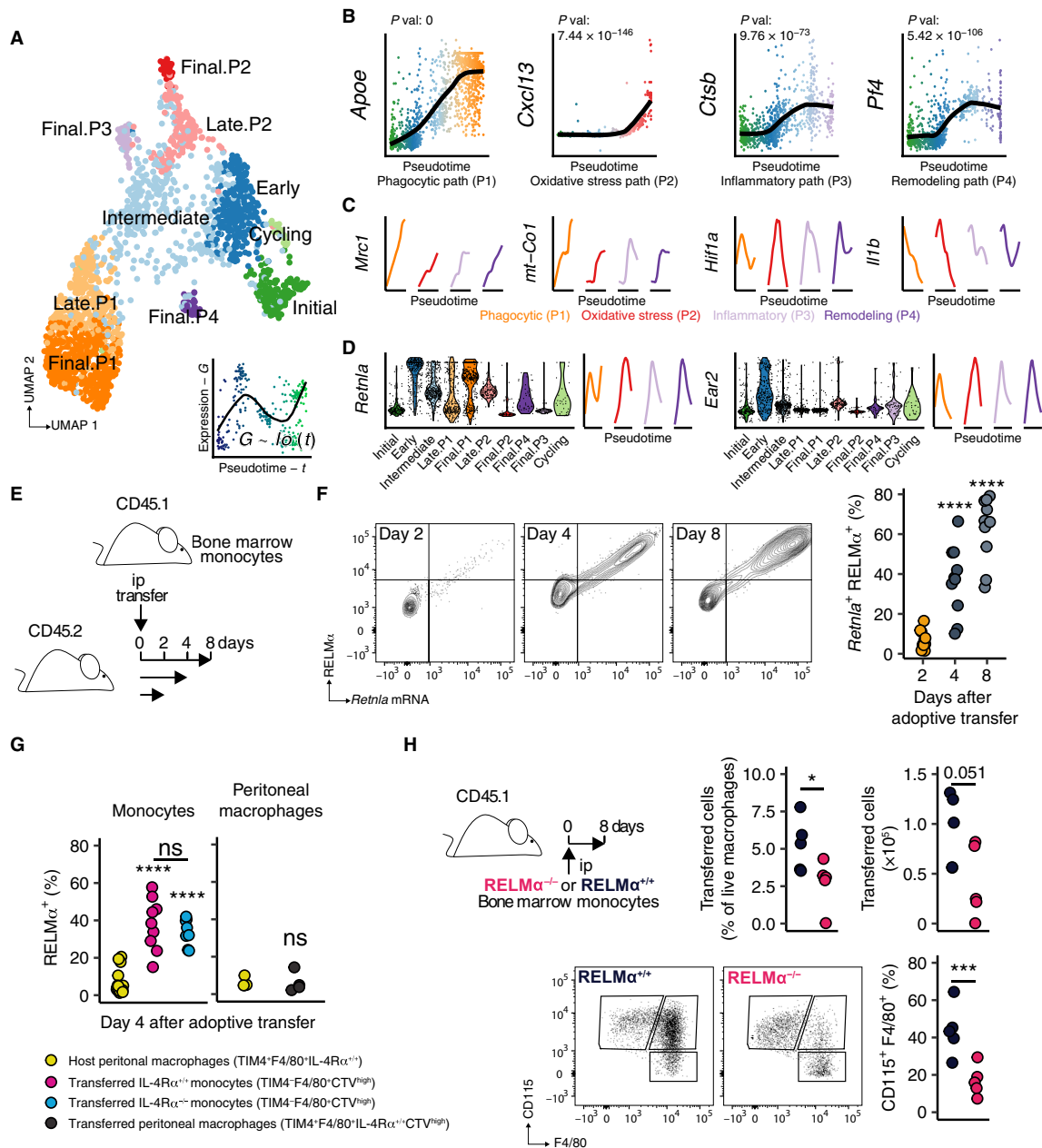
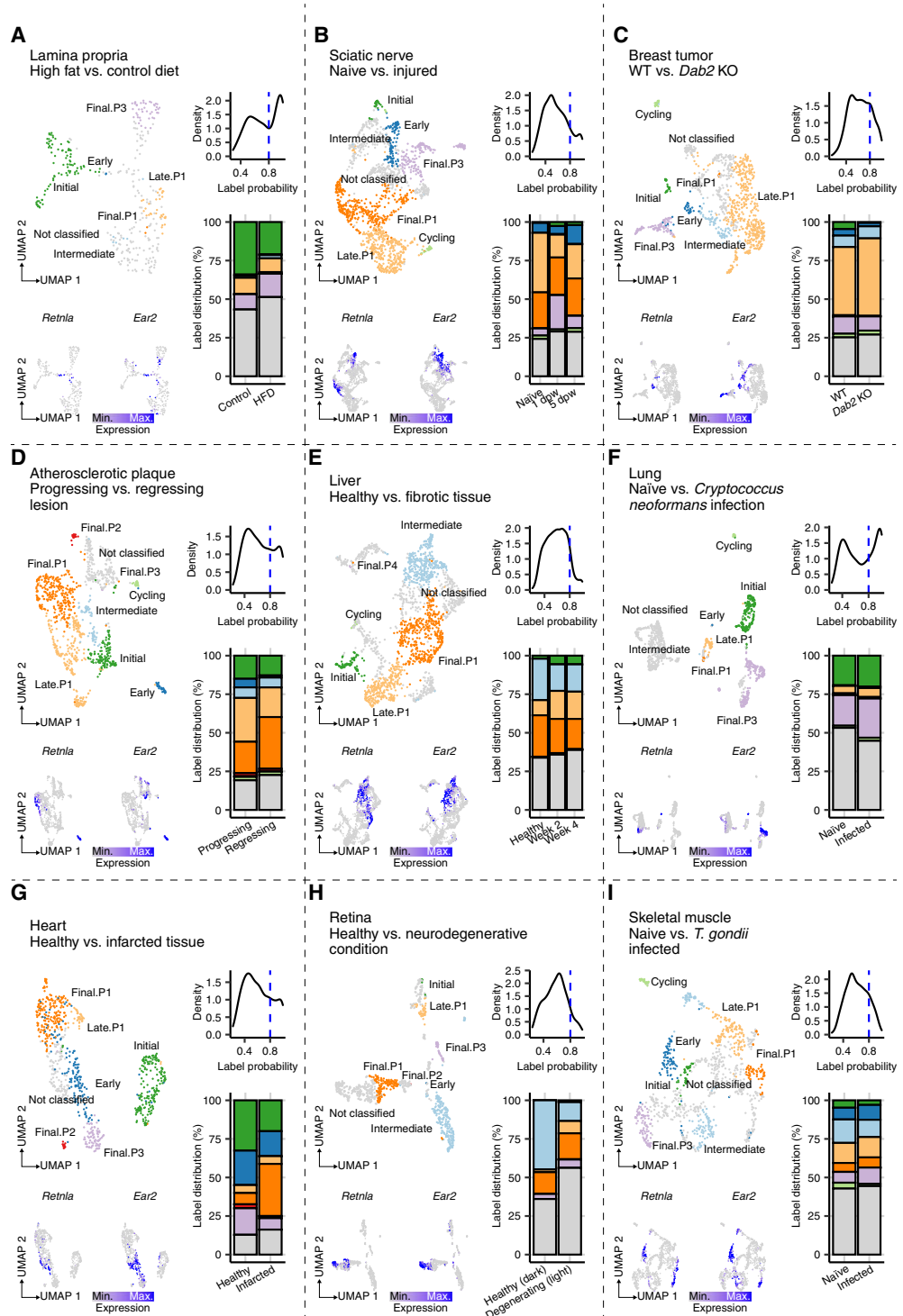


Fig. 2. Macrophage gene expression can be modeled as a function of activation, revealing a transitory stage of RELM α -expressing cells. (A) Macrophage activation stage UMAP, showing an example of a fitted general additive model (GAM) for gene expression as a function of pseudotime. (B) Top most significant GAM fits for genes associated with identified paths, showing single-cell gene expression (dots: color matching activation stage) as a function of pseudotime (x axis) for each activation path, with fitted models (black lines) and associated adjusted P values also shown. (C) Fitted GAM models (colored lines matching activation paths) of gene expression of macrophage activation markers (y axis: fixed across all paths for each gene) as a function of pseudotime (x axis: specific to each path). (D) Relative expression of RELM α coding gene *Retnla* and *Ear2* shown as violin plots for each activation stage (left) or as fitted GAM models specifically for each activation path (right). (E) Schematic view of experimental setup for adoptive bone marrow monocyte transfer from donor (CD45.1⁺) mice into the peritoneal cavity of naïve recipients (CD45.2⁺). ip, intraperitoneal. (F) Representative density flow cytometry plots (left) and quantification of percentage cells (right) expressing RELM α protein and mRNA (*Retnla*) in adoptively transferred bone marrow monocytes recovered from the peritoneal cavity of recipient mice at indicated times. Individual dots represent biological replicates from combined experiments ($n = 10$ across two repeats). Significant differences at each stage compared with day 2 are indicated (**** $P < 0.0001$) on the basis of a single-factor ANOVA followed by Tukey's honest significant differences test. (G) Quantification of percentage macrophages expressing RELM α 4 days after adoptive cell transfer within host large peritoneal macrophages, in adoptively transferred IL-4R α -sufficient (IL-4R $\alpha^{+/+}$) or IL-4R α -deficient (IL-4R $\alpha^{-/-}$) monocytes (left), or in adoptively transferred large peritoneal macrophages (right). Individual dots represent biological replicates ($n = 4$ to 18). Significant differences at each stage compared with host macrophages are indicated [**** $P < 0.0001$; ns (not significant): $P > 0.05$] or between transferred cells (ns: $P > 0.05$) based on a single-factor ANOVA analysis followed by Tukey's honest significant differences test. (H) Quantification of transferred RELM α -sufficient (RELM $\alpha^{+/+}$) or RELM α -deficient (RELM $\alpha^{-/-}$) macrophages 8 days after adoptive cell transfer (top). Representative flow cytometry dot plots of indicated markers and quantification of proportion CD115⁺F4/80⁺ cells within adoptively transferred cells (bottom) are shown. Individual dots represent biological replicates ($n = 5$). Significant differences are indicated (*** $P < 0.001$; * $P < 0.05$) on the basis of Tukey's honest significant differences test.

Fig. 3. Macrophage activation stages are conserved across tissues and inflammatory conditions. (A to I) Top left: UMAP of macrophages from indicated tissue and condition labeled according to predicted activation stage, including not classified cells (gray). Top right: Label probability distribution from indicated tissue and condition, showing confidence threshold (dashed blue line) for label assignment. Bottom right: Stage distribution shown as a percentage of total cells per biological condition, colored to match predicted labels. Bottom left: UMAP of relative expression (low, gray; high, blue) of *Retnla* and *Ear2*. Cell numbers: lamina propria, 332; sciatic nerve, 1500; breast tumor, 1000; atherosclerotic plaque, 1000; liver, 1800; Lung, 1000; heart, 773; retina, 897; skeletal muscle, 1000.



example, in the large intestine lamina propria (Fig. 3A), infiltrating initial-stage cells were abundant in steady state (Fig. 3A, bottom right) in line with the reported turnover of macrophages in this tissue (9). However, after 12 weeks of high-fat diet (HFD), the proportion of initial-stage macrophages diminished, being replaced by cells in the final.P2-stage of the inflammatory path (Fig. 3A), which is consistent with HFD-induced gut inflammation (20), and tumor necrosis factor (TNF) production by intestinal macrophages (41). This correspondence between our labeling strategy and established biology could be seen in all datasets. In sciatic nerve injury (21), a wave of inflammatory path cells (final.P3) could be seen 1 day post-wounding (dpw), which receded by day 5, when phagocytic path final.P1-stage cells took over (Fig. 3B). In breast tumors (22), the macrophage landscape was dominated by phagocytic path cells (Fig. 3C), which displayed markers of alternatively activated cells. The same appeared true in regressing atherosclerotic plaque lesions (Fig. 3D) (23) and in liver fibrosis (Fig. 3E) (24), whereas fungal infection in the lung (25) resulted in an increase in inflammatory path cells (Fig. 3F). In infarcted heart (26) and retinal damage (27), an expansion of phagocytic path cells was also evident (Fig. 3, G and H), although the diversity of activation stages in each tissue was different, with few identified stages in the retina both in steady state and after light-induced neurodegeneration (Fig. 3H).

In contrast, skeletal muscle macrophages (18) displayed diverse activation stages, with chronic parasitic infection having a modest effect on the stage distribution in this tissue (Fig. 3I), although increased inflammatory path macrophages were apparent (final.P3). Last, we observed early-stage cells, coexpressing *Retnla* and *Ear2*, in nearly all analyzed datasets (Fig. 3, A to D, G, and I), underscoring how this activation step appears to be common to macrophages in most tissues.

Despite demonstrable utility of our labeling approach, there remained a number of cells with no label assignment (i.e., not classified). We developed two potential explanations for the abundance of these cells in the studied datasets. First, our approach hinges on stringently identifying anchor pairs between the data, obtaining a high score, and/or having dominant labels in the clusters. Consequently, we are less efficient at identifying transcriptional profiles of cells in between defined activation stages. For this reason, many of the not classified cells in our analysis could be seen in between labeled clusters in the UMAP and would often share low-probability labels for flanking clusters with a more defined signature (e.g., fig. S5D, cluster 2 flanked by 1, 4, 7, and 9). Likely for this reason, intermediate-stage cells were relatively rare in query datasets, because these were the least defined transitional state that we identified in our reference data. Second, tissue-resident macrophages have a distinct transcriptional profile (4, 5) and thus might not easily relate to activated macrophages originating from circulating monocytes in inflammatory settings. We observed more unclassified cells in tissues where monocyte infiltration is rare (retina; Fig. 3H) or where specialized macrophage subsets are common (alveolar macrophages in the lung; Fig. 3F). The distinct cluster of not classified cells present on the left of the lung UMAP (Fig. 3F) was enriched for alveolar macrophage markers, thus explaining the notable bimodal label distribution in this dataset (Fig. 3F). By contrast, the label assignment in the atherosclerotic plaque dataset was nearly global (Fig. 3D) likely as only circulating monocyte-derived macrophages were studied (23).

We explored the issue of macrophage embryonic origin and tissue immune privilege in more detail by studying a dataset where microglia were recovered at different developmental steps from naïve mice (Fig. 4A and table S2) (42). In line with our expectations, we observed poor label probability distributions for all investigated ages (Fig. 4A). The probability threshold was never surpassed, and these distributions were skewed progressively toward 0 as the age of the investigated animals increased.

Together, our label transfer analysis shows that macrophages across tissues and inflammatory conditions share common transcriptional profiles that correspond to definable activation paths. Our analysis also suggests that embryonically seeded and highly specialized tissue-resident macrophages do not respond to inflammatory conditions in a way analogous to that of infiltrating monocytes, with the latter encapsulating most of the functional diversity found in all the studied datasets. Consequently, our model best captures the activation of monocyte-derived macrophages that replace tissue-resident cells during inflammation. Last, well-established paradigms of macrophage biology are reinforced by the functional stages that we defined, making these labels a potential tool to probe deeper into the functional specialization of macrophages during inflammation.

Exploiting the predictive nature of the proposed macrophage activation model

We decided to explore in greater detail potential biological insights that might be obtained from our activation model. For this purpose, we turned to the atherosclerotic plaque and breast tumor datasets (Fig. 4), both of which included interventions that ameliorated disease progression (table S2) (22, 23). Dietary and pharmacological intervention (table S2) was reported to induce regression of atherosclerotic plaque lesions (23), which are dominated by phagocytic path macrophages (Fig. 4B). There was a shift between late.P1- and final.

P1-stage cells in regressing lesions, with a sizable decrease in the proportion of late.P1-stage cells (Fig. 4C). We investigated which genes were altered in expression within cells in this activation stage between progressing and regressing lesions. We performed this analysis on the original unimputed expression data to enable our label predictions to orient the analysis without affecting the underlying measurements. We compared these regulated genes with those associated with the phagocytic path based on our pseudotime analysis (Fig. 2). Expression of all but one of the genes in this activation stage increased in regressing lesions (Fig. 4D). Moreover, all but one of these genes tended to be expressed more strongly as cells progressed from the late.P1; (Fig. 4E, dashed lines) to the final.P1-stage. Collectively, these data suggest that the intervention causing lesions to regress induced the accelerated transit of macrophages along the phagocytic path, as indicated by the increased expression of genes associated with this trajectory in late.P1-stage cells, which concomitantly decrease in abundance.

Next, we examined the breast cancer dataset, where macrophage-specific *Dab2* deletion was reported to dampen tumor progression (Fig. 4, F to J, and table S2) (22). We observed that *Dab2* was most highly expressed in phagocytic path late.P1- and final.P1-stage macrophages (Fig. 4, F and G), with the former being more abundant. We observed an increase in late.P1-stage *Dab2*-deficient macrophages (Fig. 4H), leading us to examine differentially expressed genes between these cells and their WT counterparts. Our results show that from 15 regulated genes also included in the pseudotime analysis, 11 were differentially down-regulated between these two groups (Fig. 4I). Of these 15 genes, 13 were highly expressed at this stage of activation in our reference data (Fig. 4J, dashed lines). The down-regulation of these path-associated genes and the accumulation of late.P1-stage cells could indicate that the absence of *Dab2* stalls the progression of macrophages in the phagocytic path.

Monocytes enter wounds populating the functional diversity predicted by the proposed macrophage activation model

Our model predicts that incoming monocytes are able to assume the phenotype of existing macrophages in the tissue and populate all functional stages described. In the atherosclerotic plaque dataset, all sequenced cells were derived from circulating precursors (23). To formally evaluate this, we traced the influx of monocytes into wounded skin (Fig. 5, A and B, and fig. S6). Red fluorescent monocytes (tdRFP⁺) were administered intravenously 2 or 12 dpw, and all wound macrophages were harvested 4 and 14 dpw (Fig. 5B), using index sorting to retain fluorescence values from barcoded cells for further analysis. We mapped, clustered (fig. S6A), and labeled the sequenced cells (Fig. 5A) as described above, applying similar thresholds and evaluating label probability distributions for the entire dataset (Fig. 5C) and across clusters (fig. S6, A and B). Wounded skin exhibited most previously defined activation stages, again demonstrating the robustness of our activation model.

We observed a global label probability distribution skewed toward a value of 1 (Fig. 5C), indicating a good agreement with our reference data. Moreover, label distribution across conditions was consistent with expectations based on established literature (43), with an early wave of inflammatory cells at 4 dpw (Fig. 5D) and a later increase in phagocytic path cells at 14 dpw (Fig. 5D). Transferred monocytes were detected at both 4 and 14 dpw (fig. S6C), although only when given on day 2 (fig. S6D). Infiltrating monocytes were distributed across all detected clusters and assigned stage

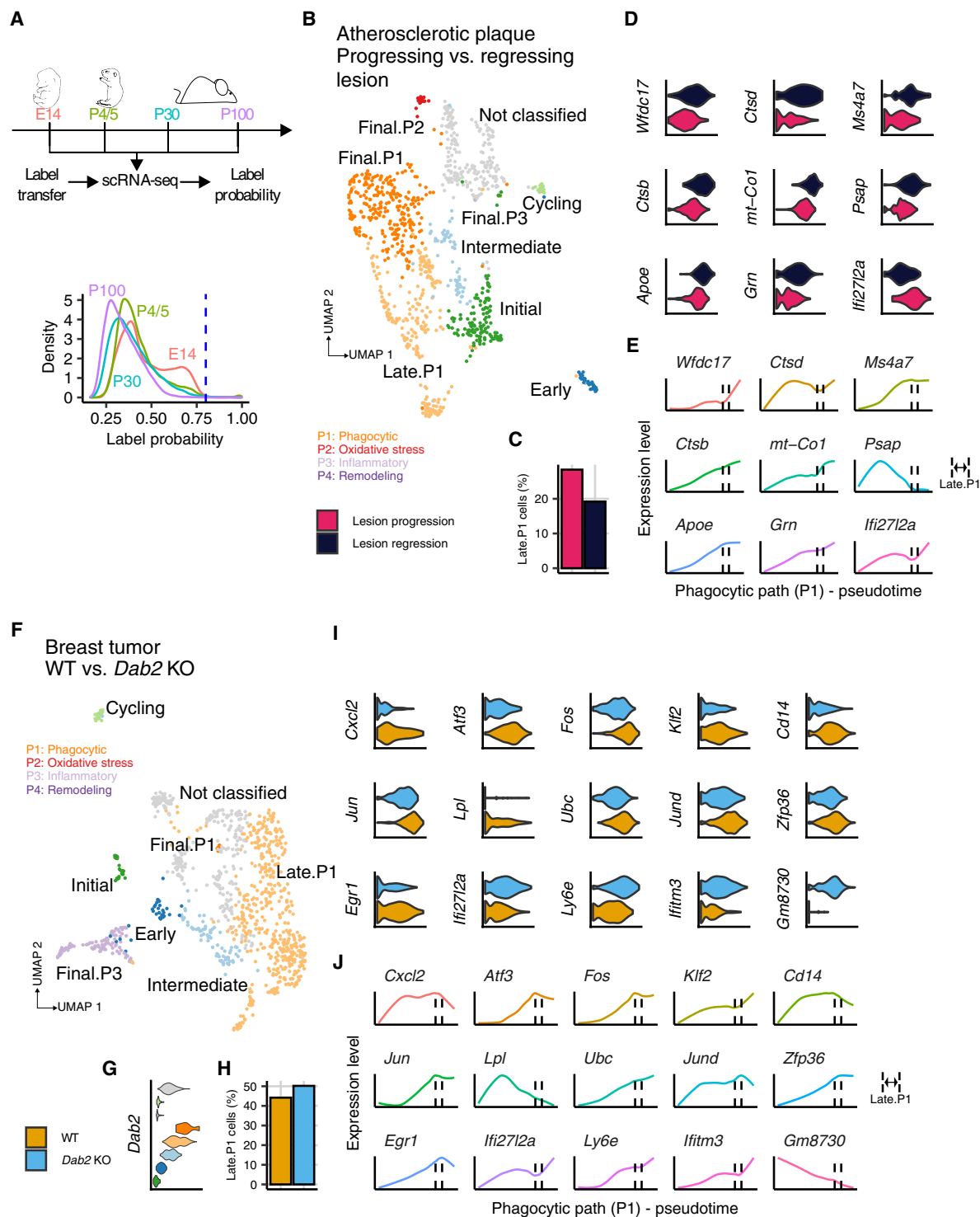


Fig. 4. Dysregulation of path-associated gene expression results in pathological macrophage activation stalling. (A) Label probability distribution of microglial datasets obtained from mice at indicated developmental stages. (B) UMAP with stage labels from macrophages obtained from atherosclerotic plaque regressing (black) and progressing (dark pink) lesions. (C and H) Percentage of late.P1 cells per biological condition. (D) Significantly (adjusted $P < 0.01$) regulated genes (log fold change > 0.25) in progressing compared with regressing lesion macrophages. (E and J) Fitted GAM models for expression of differentially regulated genes (y axis) as a function of phagocytic path pseudotime (x axis) indicating late.P1 stage (dashed vertical lines). (F) UMAP with stage labels from macrophages obtained from spontaneous breast cancer tumors in animals with a macrophage-specific *Dab2* deletion (*Dab2* KO, light blue) and WT littermates (orange). (G) Violin plot of relative *Dab2* expression across activation stages. (I) Significantly (adjusted $P < 0.01$) regulated genes (log fold change > 0.25) in *Dab2* KO compared with WT macrophages.

labels (Fig. 5, E to G) mirroring closely the distribution for all macrophages sequenced (Fig. 5, D and G). As predicted by our model, fluorescent cells were assigned to the initial stage and inflammatory path 4 dpw (Fig. 5G), emphasizing the transitory nature of the early inflammatory wave that occurs during tissue repair. By contrast, transferred monocytes mapped preferentially to the early stage and phagocytic path 14 dpw (Fig. 5G). The fact that transferred cells only mapped to the initial stage on day 4, and that by day 14 they had assumed other identities, reflects the number of days since these cells accessed the wound and supported our model, showing monocyte flux through distinct activation stages. More early-

stage macrophages coexpressing *Retnla* and *Ear2* were detected at 14 dpw (Fig. 5, G and H) compared with day 4, despite the presence of inflammatory path cells at this time point that, according to our model, should have transited through the early stage. Previously, 2 days were insufficient to observe *Retnla* expression in infiltrating cells (Fig. 2F), and increased proportion of early-stage cells at 14 dpw (Fig. 5G) aligns with our earlier findings that, after 8 days, a higher percentage of infiltrating cells would fall in this stage (Fig. 2F). To reconcile these observations, we propose that the relative speed at which macrophages traverse defined activation paths is influenced by the inflammatory conditions at the site of immunological insult,

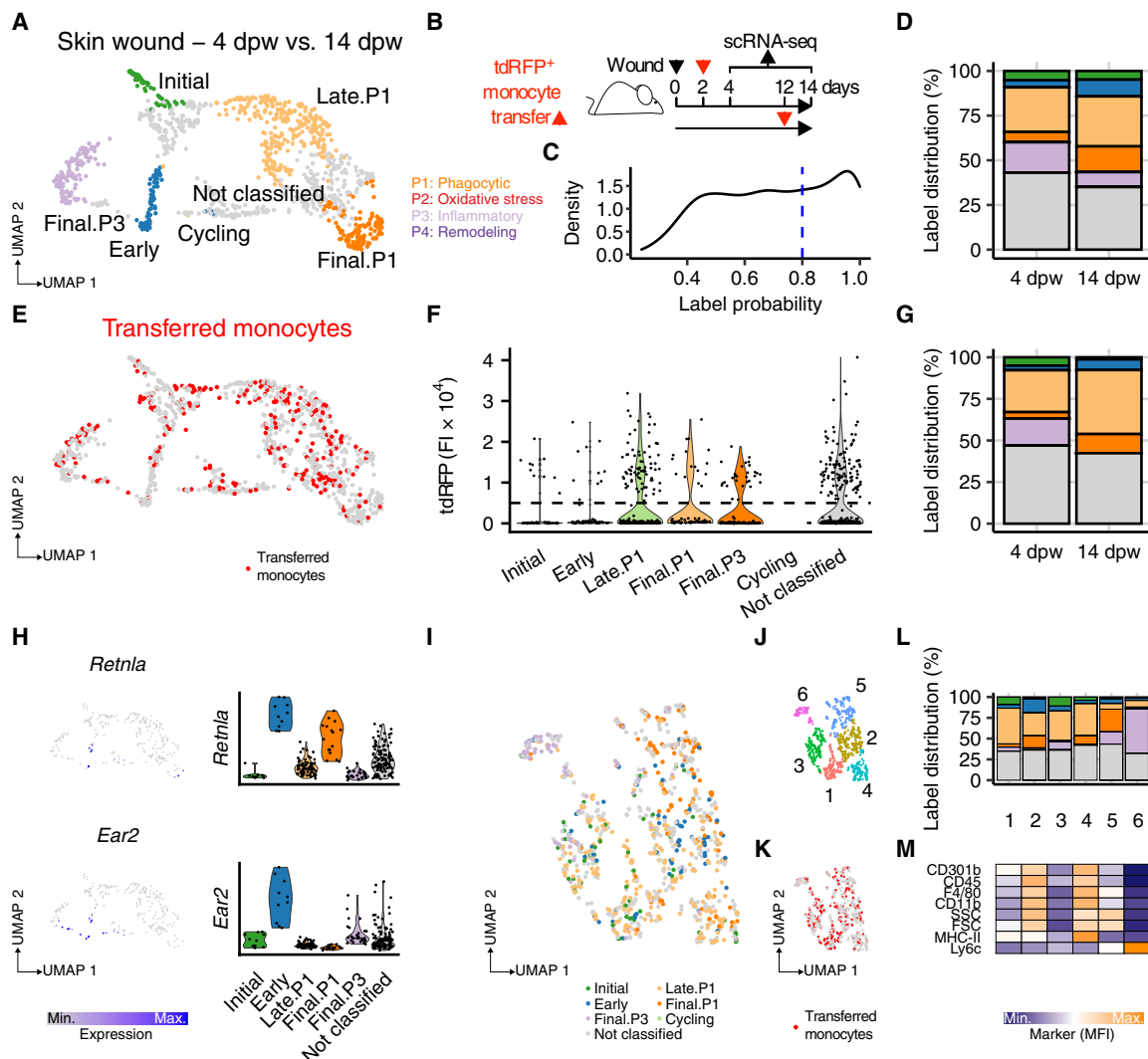


Fig. 5. Wound macrophage recruitment confirms activation path model. (A) UMAP with stage labels from macrophages (cells = 1061) obtained from wounded skin biopsies 4 and 14 dpw ($n = 5$ to 9). (B) Schematic overview of experimental setup for adoptive tdRFP⁺ monocyte transfer into wounded animals. (C) Label probability distribution showing confidence threshold (dashed blue line) for label assignment. (D) Stage distribution shown as a percentage of total cells per biological condition, colored to match predicted labels. (E) UMAP with tdRFP⁺ monocytes labeled in red. (F) tdRFP⁺ fluorescence intensity (FI) in all cells across predicted labels. FI threshold for transferred cell detection is indicated as a dashed line. (G) Stage distribution shown as a percentage of total tdRFP⁺ cells per biological condition, colored to match predicted labels. (H) Relative expression (low, gray; high, blue) in tdRFP⁺ cells of *Retnla* and *Ear2* shown as UMAPs (left) and as violin plots for each activation stage (right). (I to K) UMAP calculated on the basis of indexed flow cytometry data, labeled with predicted activation stages (I), k-means clustering (J), or tdRFP⁺ monocytes (K). (L) Stage distribution shown as a percentage of total cells per flow cytometry cluster, colored to match predicted labels. (M) Relative mean fluorescence intensity (MFI; low, blue; high, orange) in flow cytometry clusters.

so that cells may accelerate their passage through identified stages to better adapt to the required immune response.

Next, we took advantage of the indexed nature of the skin wound dataset to validate our labeling strategy with common macrophage phenotypic markers. For this purpose, we scaled the fluorescent signal of CD301b, CD45, F4/80, CD11b, MHC-II, and Ly6C, as well as the side and forward scatter parameters, across all cells and calculated a UMAP from this flow cytometry data, retaining the stage labeling based on the transcriptional profile of the cells (Fig. 5I). We then identified clusters using k-means (Fig. 5J and fig. S6E). We observed that late.P1-, final.P1-, and final.P3-stage cells each dominated a cluster (Fig. 5L, clusters 4, 5, and 6, respectively), whereas early-stage cells localized predominantly to cluster 2 (Fig. 5, J and L). As expected, transferred monocytes were evenly distributed across these clusters (Fig. 5K and fig. S6F), further emphasizing the ability of these cells to differentiate into all identified functional stages. Last, we show that these flow cytometry-based clusters are associated with significantly different protein expression levels ($P < 0.001$; Fig. 5M). Collectively, these data show that monocytes entering a wound respond to this environment by becoming activated in accordance with the model proposed in this study and provide surface protein validation of these stages.

Macrophage activation stages in tissues have distinct transcriptional markers

Our approach relies on the quality of anchor pairs identified across datasets to transfer labels and impute gene expression data. In this manner, we identified all activation stages in different proportions across all the datasets studied (Fig. 6A). Because this approach by necessity transforms the original expression data, we sought to determine its robustness by interrogating labeled cells directly (Fig. 6B). For this purpose, we took all high-label probability cells (>80%) from 10 query datasets and combined these with a randomly sampled portion ($n = 500$) of macrophages from our reference, retaining only the label assignment and original uncorrected gene expression data (Fig. 6B). Once extracted, these macrophages ($n = 2843$) were integrated across tissues, without giving priority to any dataset, and then clustered and visualized as a UMAP (Fig. 6C).

Our expectation for this analysis was that the transcriptional tissue signature would not obscure the activation stage label. That is, our model would predict that tissues would not define the resulting cell clustering but rather that the activation stage of these cells would be sufficient to group them in this unsupervised analysis. Critically, this was the outcome that we observed (Fig. 6D). Cells with identical activation labels clustered together, regardless of the tissue of origin or the inflammatory condition, demonstrating that our initial approach was valid. We next performed a complementary trajectory inference analysis on this data using Monocle (44), which organized cells into two main branches of macrophage activation, chiefly one directed to the phagocytic path (P1) and one toward the inflammatory pathways (P2 and P3) (fig. S7A). Although this analysis is unable to resolve the differences between P2 and P3, the overall architecture of the projection is reminiscent of our reference data. Cells in the initial, early, and cycling stage clustered near each other, while intermediate-stage macrophages separated the bottom phagocytic and remodeling paths from the oxidative stress and inflammatory paths at the top of the UMAP (Fig. 6D). This distribution of clusters adds weight to our proposed activation trajectories and emphasizes the relative relationship between the activation stages defined.

Having all macrophages clustered in this manner allowed the extraction of tissue-independent transcriptional markers for all activation stages. We found up-regulated genes (Fig. 6E and data file S2) corresponding to each identified activation stage, which largely aligned with the genes that we originally associated with each label (fig. S2C and data file S1). Moreover, we extracted from this result potential cell surface markers (data file S3) and selected those with commercially available antibodies (Fig. 6F and fig. S7B). We reasoned that combining these markers would enable us to identify macrophages at different activation stages. We injected the peritoneal cavity of mice with 10^6 CFU of *L. mono* and tracked macrophage recruitment 1, 4, and 8 days p.i. (Fig. 6G). The resulting fluorescence intensities for the macrophage populations were scaled using a linear regression model and used to cluster cells and calculate a principal components analysis and UMAP for visualization (Fig. 6H). These scaled fluorescence values were relative to the cells retained in the analysis, so rather than positive or negative, we used high (hi) or low (lo) to score protein expression. This analysis was able to capture a high degree of heterogeneity in the population of macrophages in the peritoneal cavity (Fig. 6H and fig. S7C), with cells originating from different time points after infection clustering separately. Next, we assigned our model's activation stage labels to the identified clusters based on the distinct staining patterns that we observed in the data (fig. S7C). For some markers, we found no correlation between transcript and protein levels (*Nrp1*, CD304; *Fcgr4*, CD16-2; *Cd14*, CD14; *Tnf*, TNF); however, we were reasonably confident of the annotation based on the remaining markers and identified at least three proteins that are distinctly expressed in each of the identified activation stages (Fig. 6H, right, and fig. S7C).

Next, we used the assigned labels to explore the population dynamics across our experimental peritonitis model (Fig. 6I). Our annotation was consistent with the population dynamics that our model would predict and are expected of an inflammatory process (Fig. 6I). We observed a wave of initial-, early- and late.P2-stage macrophages replacing the tissue-resident cells shortly after infection, followed by a progressive appearance of cells in the intermediate-stage, and lastly an accumulation of final.P2-, final.P3-, late.P1-, and final.P1-stage cells (Fig. 6I). RELMa expression was greatly enriched in the early-stage macrophages, which were most abundant 4 days p.i. (Fig. 6H). These findings provide further support to our proposed model, and the identified markers may be used by researchers to explore macrophage heterogeneity in other contexts.

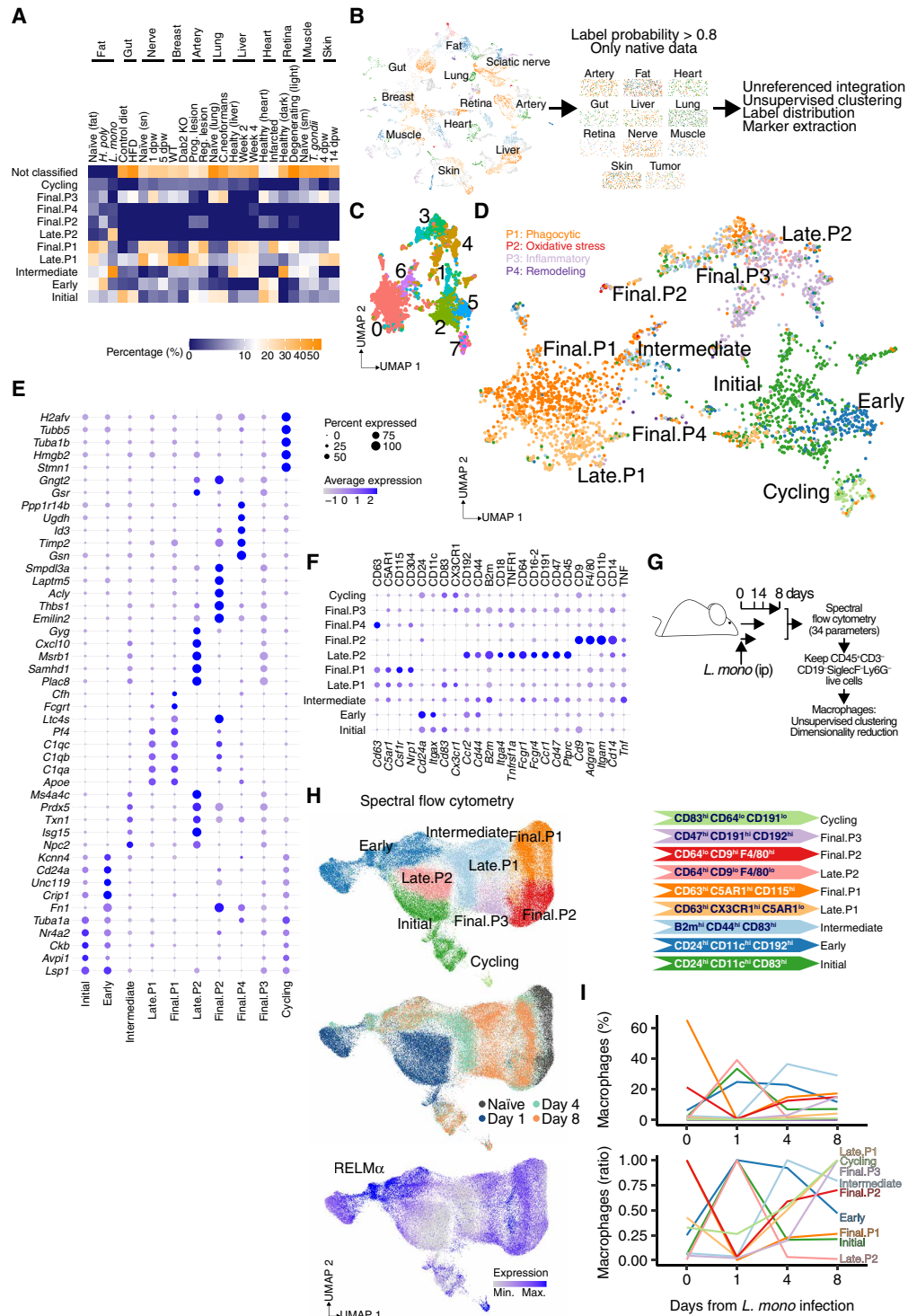
Transcriptional network analysis reveals information hubs and upstream regulators

Earlier, we hypothesized that changes in the regulation of genes associated with defined activation paths were likely to stall or promote macrophage activation. To explore this final aspect of the data, we returned to the pseudotime-regulated genes (Fig. 2) and built and then filtered a network based on known protein-protein interactions and gene expression regulation along identified paths (fig. S8, A and B). Next, we clustered the resulting network, performed Gene Ontology (GO) term enrichment analysis in each cluster (fig. S8C) and labeled the network according to the most enriched term in the gene set. The resulting network (Fig. 7A, 242 genes) showed 10 clusters associated with distinct functions. These gene sets were not engaged similarly by all activation paths, as revealed by subsetting the network to include only genes significantly associated with pseudotime in each path (Fig. 7B).

Fig. 6. Cross-condition data integration reveals stage-specific marker genes.

(A) Activation stage distribution shown as percentages of total cells per biological condition and tissue. Scale was modified with a square-root transformation for ease of visualization. (B) Schematic overview of data reprocessing strategy. (C and D) Integrated UMAP of macrophages (cells = 2843) across conditions and tissues labeled with identified clusters (C) or previously assigned activation stages (D). (E) Dot plot of top significantly (adjusted $P < 0.01$) regulated genes (log fold change > 0.25) across activation stages. (F) Dot plot of top significantly regulated genes associated with GO term "Cell surface" (GO:0009986) across activation stages selected for flow cytometry analysis. Gene (bottom) and protein (top) names are shown. (G) Schematic view of experimental peritonitis. (H) UMAP calculated on the basis of spectral flow cytometry data for macrophages from naïve mice, or after 1, 4, and 8 days of *L. mono* intraperitoneal injection. Cells are colored according to assigned stage (top), sample group (middle), or RELM α FI (bottom). Proposed gating markers for each assigned stage are infected (right). Data were concatenated from 10,000 macrophages per independent biological replicate ($n = 11$). (I) Population dynamics across samples indicated as a mean percentage of total macrophages (left) or scaled for each population ($\frac{\text{Mean \% stage } i}{\text{max}(\text{Mean \% stage } i)}$).

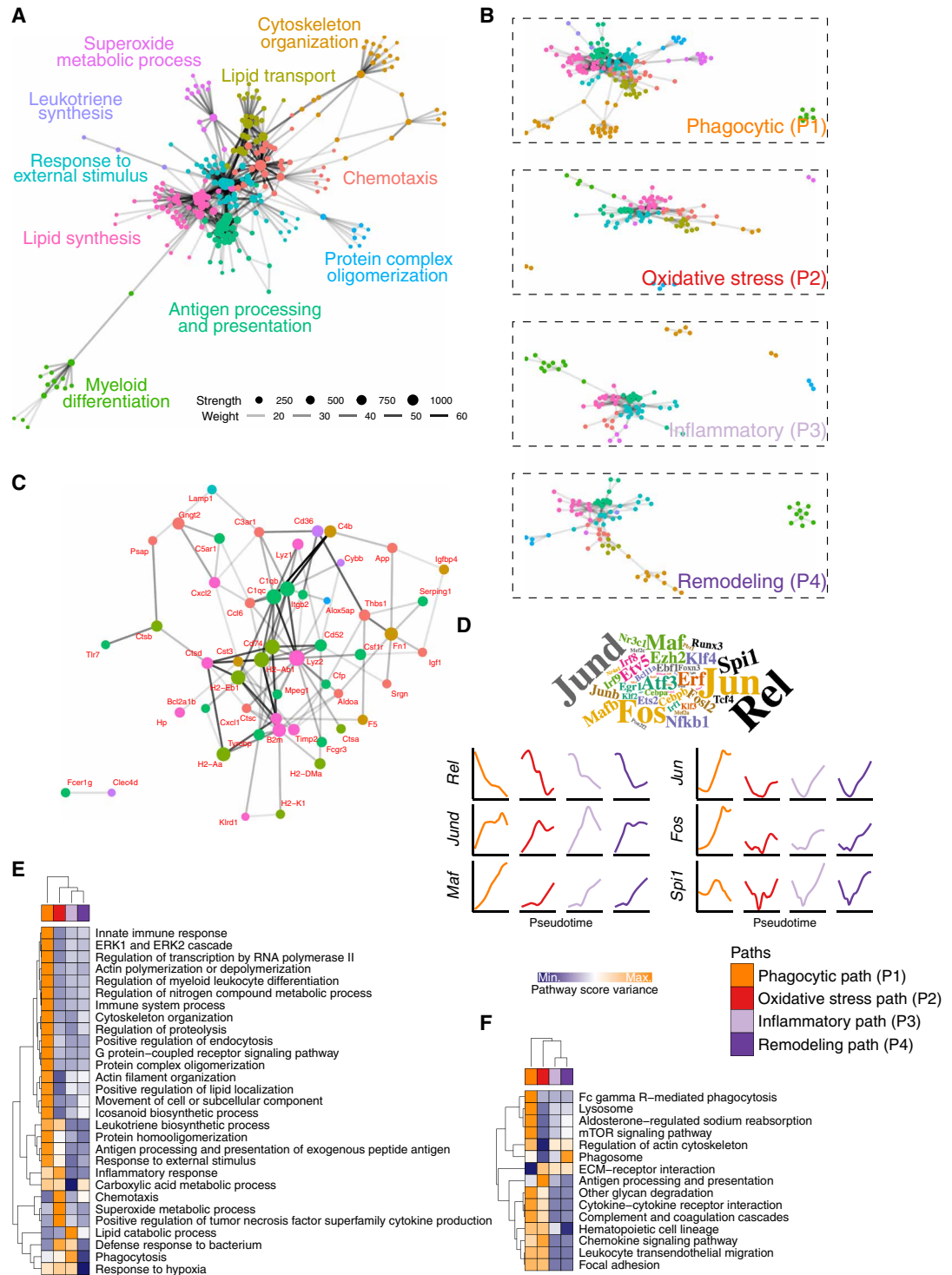
We extracted three types of information from this transcriptional network. First, we examined highly connected nodes, which articulated the network by connecting two or more clusters and were overrepresented in the paths connecting pairs of nodes in the network (i.e., high betweenness). Examining genes meeting these criteria (Fig. 7C) highlighted not only some well-known macrophage regulators (e.g., *Lyz2* and *Csf1r*) but also genes whose function has not been widely studied in the context of macrophage activation (e.g., *Gngt2* and *Srgn*), thus warranting further exploration. Second, we identified transcription factors (TFs) upstream of the transcriptional network clusters (Fig. 7D), of which six (*Rel*, *Maf*, *Fos*, *Jun*, *Spi1*, and *Jund*) were themselves regulated dynamically along the activation paths. Some TFs had opposing behaviors (*Rel* versus *Maf*), whereas others behaved similarly in all paths



except one, where they suddenly veered in opposing directions (*Spi1* versus *Fos/Jun*). Last, we took the top three GO-enriched terms in each cluster (Fig. 7E and fig. S8C) and all enriched Kyoto Encyclopedia of Genes and Genomes (KEGG) pathways detected (Fig. 7F) and calculated gene set scores for each of these (table S1). We then estimated the variance of each gene set score within the activation paths and represented these data as a heatmap (Fig. 7, E and F), finding

Fig. 7. Macrophage transcriptional network across activation paths.

(A) Transcriptional network of protein-protein interactions, depicting genes ($n = 242$) as nodes and interactions as edges ($n = 716$). Node size corresponds to calculated strength. Node color is associated with the assigned network cluster. Edge opacity corresponds to calculated weight of interaction. The most enriched GO term associated with each cluster is indicated. **(B)** Transcriptional network as in (A), but split along activation paths, with arbitrary node size and edge opacity. **(C)** Transcriptional network as in (A), limited to nodes with high betweenness (75% quantile) that connect two or more clusters. Gene names indicated in red. **(D)** Top: TF enrichment analysis shown as a word cloud where size of name is proportional to the number of gene sets in transcriptional network clusters associated with the specific TF. Bottom: Fitted GAM models (colored lines matching activation paths) of gene expression of enriched TFs (y axis: fixed across all paths for each gene) as a function of pseudotime (x axis: specific to each path). **(E and F)** Heatmap showing relative gene set score variance (low, blue; high, orange) of enriched GO terms (E) or KEGG pathways (F). mTOR, mammalian target of rapamycin; ERK1, extracellular signal-regulated kinase 1.



a distinct profile for each path for these functions. In this manner, we highlight the relative regulation of several processes of interest in the activation paths that we defined, as a guide to researchers wishing to explore these aspects of macrophage function in more detail.

In summary, we used a predictive model of label transfer to encompass macrophage activation irrespective of tissue or inflammatory

condition. We demonstrate that this model is robust, aligning with well-established paradigms of macrophage function, while providing original avenues for investigation. We provide surface and global gene expression profiles for these activation stages to aid in their identification in future studies. We have prepared an online tool (<https://t.jh.edu/macrophage-framework>) to aid in exploring the data

contained in this study. Our results emphasize the conservation and relative homogeneity of macrophage activation across tissues, transcending macrophage tissue residence, while still allowing for activation diversity.

DISCUSSION

Advances in the understanding of macrophage ontogeny and of differential gene expression signatures linked to macrophage tissue residence have revealed inherent complexity within this cell type. Moreover, the transcriptional profile of macrophages after exposure to a broad range of stimuli for which they are known to express receptors revealed a spectrum of potential activation states not captured by in vitro models. In light of these findings, it has become difficult to relate macrophage activation across investigations. Our study offers an alternative view of macrophage activation in tissues during inflammation. By comparing the transcriptional profiles of macrophages recovered from different tissues from mice experiencing distinct diseases/conditions, we identified a limited and consistent number of transcriptional profiles that were unobscured by the tissue or stimulus studied. We modeled these conserved and yet diverse signatures as stages across four activation paths, finding that phagocytic and inflammatory paths were most common. These paths have features in common with M2 and M1 respectively, encompassing those references while offering a broader and dynamic alternative. Last, our analysis offers insights into the information hubs, TFs, and gene expression programs that are responsible for shaping macrophage function.

The macrophage activation model that we propose, where cells transit through an initial and early stage of commitment to a particular path, is evident in other independent analyses. For instance, in a murine model of nonalcoholic steatohepatitis (NASH) a monocyte-derived population of Ly6C^{lo} macrophages expressed high levels of *Ccr2*, *Klrd1*, and MHC-II (45), comparable with genes expressed in initial-stage cells in our analysis (data file S1 and <https://t.jh.edu/macrophage-framework>). *Ccr2* expression in particular gives credence to our choice of starting point for the model because this encodes a critical tissue-homing receptor in circulating monocytes (46). A closely associated cell population in the NASH dataset expressed both *Ear2* and *Fn1*, mirroring early-stage macrophages (data file S1). Moreover, in the context of this disease, this population gave rise to Kupffer cells (45), which expressed high levels of *Mrc1*, *Apoe*, and complement-associated genes, similarly to phagocytic path macrophages. Another instance where this progression is evident is in joint synovial macrophages (47). In this setting, two populations of interstitial macrophages, one MHC-II^{high} and one RELMα⁺ reminiscent of the initial- and early-stage cells described here, respectively, replenished long-lived synovial tissue-resident cells (47). The possibility to reconstruct our model in these independent analyses demonstrates the robustness and universality of our findings.

Our model highlights the role of incoming monocytes into tissues, both under homeostasis and inflammatory conditions. The input of monocyte-derived macrophages to the overall tissue macrophage pool during homeostasis varies from organ to organ (4), and under these conditions, we found that the contribution of the four identified activation paths was diverse between tissues, likely as a result of microenvironmental signals that are themselves heterogeneous. Thus, our data indicate that the commitment of monocytes to these activation paths is regulated not only by the inflammatory settings,

which invariably altered the proportion of cells in each stage, but also by the specific nature of the tissue. We further demonstrated that the emphasis of our model on monocyte-derived macrophages was likely due to the distinct transcriptional profile of embryonically derived macrophages (2), which were labeled as not classified in our analysis. One implication of this finding is that incoming monocytes give rise to most of the functional diversity in any given tissue, whereas the resident cells remain more transcriptionally stable regardless of the insult. Similar conclusions were drawn recently (10) from observations on alveolar macrophages, which have been shown to be less plastic, less phagocytic, more permissive to infection, less responsive to IL-4 stimulation, and generally less engaged in ongoing local immune responses than are monocyte-derived cells (48–50). Tissue-resident macrophages in other tissues, specifically the peritoneal cavity, have also been shown to be less immunologically active (51), even if they are highly proliferative (52). Likewise, monocyte-derived macrophages have been shown to play a dominant role in tumors (53). The mechanisms restricting tissue-resident macrophage activation have not been elucidated, although epigenetic imprinting (1, 10) and autophagy-enforced quiescence (54) are likely candidates. Overall, the emerging picture is one where macrophage functional plasticity in response to a loss of homeostasis within tissues is a feature of cells derived from recruited monocytes, which participate in the induction and resolution of inflammation by moving along defined activation paths. This view does not exclude the possibility that tissue-resident macrophages are contributing to the response to tissue damage, but it does predict that monocyte-derived cells are the major contributors in this regard. In addition to this limitation, we did not explore datasets originating from viral infections, which could give rise to different transcriptional profiles. Furthermore, our analysis is largely based on data from one strain of mice (C57BL6), and it remains to be seen how fully the findings can be recapitulated in other mouse strains or species.

In our model, we postulate that macrophages become activated through four possible paths, and we infer that only cells in the phagocytic path go on to replace tissue-resident macrophages. Several independent lines of investigation support this hypothesis: Increased expression of complement genes has been reported in Kupffer cells (45) and alveolar macrophages (55) derived from monocytes; phagocytosis appears to be a key feature of tissue-resident macrophages (56); phagocytic receptors like *Mrc1*, *Cd163*, *Timd4*, and *Mertk*, all highly expressed in phagocytic path cells, are associated with tissue-resident macrophages (56). It is possible that through phagocytosis, macrophages become tissue imprinted. Thus, by engulfing apoptotic cells, macrophages might indirectly absorb factors that convey tissue identity.

By far, the most abundant gene signature that we observed in our analysis was that of the later stages of the phagocytic path. As mentioned above, this transcriptional profile is evident elsewhere (45, 55). During lung fibrosis, *Apoe* and complement gene expression became dominant features of disease progression (19). This gene signature can be extended to human macrophages involved in injury resolution (57). Our proposal that these cells give rise to tissue-resident macrophages explains in part this relative abundance. However, their transcriptional profile also overlaps with genes associated with alternative activation (16). Moreover, the complement product *C1q* has been linked to macrophage proliferation (58), a characteristic of alternatively activated macrophages. It is intriguing that

these macrophages are critical to restoring homeostasis by removing dead cells, which boosts their IL-4–driven phenotype (59), yet they also have a clear role in the pathology of several of the conditions explored herein. Our findings suggest that stalling macrophages along the phagocytic path can be both beneficial, as seen in the case of breast tumors, and detrimental, as observed in atherosclerotic plaques (Fig. 4). Even tissue-imprinted pathogenic microglia associated with Alzheimer's disease converged into an *ApoE*-expressing phenotype (60). On the basis of this, we postulate that determining how to manipulate progression along the phagocytic path may offer therapeutic opportunities.

Although in-depth identification of the drivers of macrophage transit through the proposed activation paths is beyond the scope of this study, our initial exploration of the data revealed 242 highly interconnected genes with some common upstream regulators and mapping to diverse functions. How this transcriptional network is shaped within each tissue will be of great interest moving forward. However, the fact that the number of macrophage activation stages that we defined was conserved and limited, despite the diversity of insults and tissues studied, suggests that common undercurrents guiding macrophage activation might be built into tissues. One potential set of candidates for orchestrating these processes would be signals associated with tissue damage, which is ubiquitous during inflammation. The production of alarmins by stromal cells leading to the activation of resident innate immune cells [e.g., type 2 innate lymphoid cells (ILC2s) and mast cells] might be an important driver of macrophage tissue engraftment, in particular because the signals that they produce are capable of guiding both pro- and anti-inflammatory phenotypes. Thus, seemingly opposing signals (i.e., IL-4, TNF, IL-1 β , IL-10, IL-13, and prostaglandin E₂) produced concomitantly by tissue-embedded mast cells (61, 62) and ILC2s (63) might be partly responsible for the diversity of observed macrophage activation paths in all conditions. It is feasible that additional signals provided by metabolites (64) might contribute to these outcomes.

In particular, as we move into the era of single-cell genomics, establishing a lingua franca that allows us to describe macrophage biology in humans and other animals, and across tissues and diseases, is critical. Not only is this a matter of transferring insights from one study to another but also in shaping our understanding of the function of macrophages in vivo, especially in inflammatory diseases. Moreover, moving the focus away from individual genes and toward gene signatures might allow for better transferability of findings between mouse and human models. Our data readily find parallels in human conditions (57). Last, understanding how the local micro-environment shapes the immune response is possible only if we are able to define the common threads of that response in the first place. In this context, our approach highlights the overarching similarity that can be found in the way in which macrophages diversify their function, without dismissing the influence that inflammatory conditions and tissue niches impose on that functionality. We consider our approach is a step toward building a common framework to describe macrophage activation that can be applied broadly to explore the biology of these important cells.

MATERIALS AND METHODS

Study design

The objective of this study was to integrate the transcriptional profile of macrophages retrieved from diverse inflammatory conditions

and in steady state. We used scRNA-seq technologies and flow cytometry to study cells ex vivo. Tissues were obtained from animals infected with several pathogens, wounded or fed experimental diets. We adoptively transferred monocytes and phenotyped these and other macrophages after specified times. Collected data were analyzed with bioinformatic and computational tools with the goal of developing a unified framework for monocyte-derived macrophage activation. Group sizes and end points were determined on the basis of experimental purposes using previous experience or estimated on the basis of preliminary data and expected power of 95%. No outliers were detected in the data. Age- and sex-matched mice were assigned randomly to experimental groups. This study was not blinded. Sampling and experimental replicates are indicated in each figure legend.

Mouse models

C57BL/6 J [Research Resource Identifier (RRID): IMSR_JAX:000664], B6.129P2-Lyz2^{tm1(cre)lfo/j} (RRID: MGI:5014089), CD45.1 congenic (RRID: IMSR_JAX:002014), and C57BL/6 N (RRID: MGI:5882504) mouse strains were purchased from The Jackson Laboratory. IL-4R α ^{-/-} mice were generated from B6.129P2-Lyz2^{tm1(cre)lfo/j} and B6-Il4ra^{tm1(loxp)} (65). Mice were maintained at the Max Planck Institute for Immunobiology and Epigenetics or at the Bloomberg-Kimmel Institute for Cancer Immunotherapy at Johns Hopkins. C57BL/6J (RRID: MGI:2670020) and R26^{LSL-tetRFP} (66) mice were maintained at the Experimental Center of the Medical Faculty, TU Dresden. Bone marrow from RELM α -deficient animals was donated by M. Nair from University of California Riverside. Animal care was undertaken in accordance with Institutional Animal Use and Care Guidelines with approval by the corresponding animal care committee. All animals used for tissue harvest or experimental procedures were aged between 6 and 9 weeks at the start of the experiment. Animals were humanely euthanized by carbon dioxide asphyxiation followed by cervical dislocation and tissue dissection. Mice were bred under specific pathogen-free standards.

Experimental infections and diets

L3 infectious-stage *H. poly* larvae were provided by J. Urban Jr, U.S. Department of Agriculture, Agricultural Research Service, Beltsville Human Nutrition Research Center, Diet Genomics and Immunology Laboratory, Beltsville, USA. To induce *H. poly* infection, mice were gavaged with 200 L3 infectious-stage larvae in phosphate-buffered saline. Mice were left for 13 days before being euthanized. A WT strain of *L. mono* was used for infections. Mice were infected subcutaneously on the footpad with a sublethal dose of 1×10^6 colony-forming units (CFU). Mice were left for 1 day before being euthanized. Alternatively, mice were injected intraperitoneally 1×10^6 CFU and left for 1, 4, or 8 days before being euthanized. Obesity was induced by ad libitum feeding of C57BL/6 mice for 12 week with irradiated HFD (rodent diet 60% kcal from fat; catalog no. D12492, Research Diets Inc.). Control diet (chow) containing 24% protein, 47.5% carbohydrate, and 4.9% fat was given to age- and sex-matched animals as a control group. Cells were isolated from tissues obtained from euthanized animals (see Supplementary Methods). Single live cells were purified via fluorescence-activated cell sorting, excluding dead cells labeled with LIVE/DEAD dyes (Thermo Fisher Scientific) and doublets based on side and forward light scatter. Lamina propria cells were further sorted on the basis of CD45 expression (BioLegend, clone: 30-F11).

Monocyte/macrophage isolation and transfer

Monocytes were isolated from bone marrow using with MojoSort Mouse Monocyte Isolation Kit (BioLegend) following the manufacturer's instructions or via fluorescence-activated cell sorting using fluorochrome-conjugated monoclonal antibodies: CD11b (BioLegend, clone: M1/70), F4/80 (Biozol, clone: BM8), SiglecF (BD Horizon, clone: E50-2440), Ly6G (BioLegend, clone: 1A8), CD11c (BioLegend, clone: N418), MHC-II (BioLegend, clone: M5/114.15.2), and Ly6C (BioLegend, clone: HK1.4). Macrophages were isolated from peritoneal lavage via magnetic sorting using biotinylated monoclonal antibody against T-cell immunoglobulin and mucin domain containing 4 (TIM4) (Miltenyi Biotec, clone: REA999), and Anti-Biotin MicroBeads (catalog no. 130-090-485, Miltenyi Biotec) following the manufacturer's instructions. Isolated cells were stained with Cell-Trace Violet (Life Technologies), assessed for purity via flow cytometry, and then 0.5×10^6 to 1×10^6 cells per mouse were transferred via intraperitoneal injection to littermates randomly assigned to experimental groups. RFP⁺ monocytes were isolated from B6.RFP mice via immuno-magnetic depletion of whole bone marrow by incubating samples with biotinylated antibodies against CD3 (eBioscience, clone: 145-2C11), CD4 (eBioscience, clone: GK1.5), CD8 (eBioscience, clone: 53-6.7), CD45R (BioLegend, clone: RA3-6B2), CD19 (eBioscience, clone: eBio1D3), NK1.1 (eBioscience, clone: PK136), Ter119 (BioLegend), CD49b (BioLegend, clone: DX5), Ly6G (BioLegend, clone: 1A8), and CD117 (BioLegend, clone: 2B8). Anti-Biotin MicroBeads (Miltenyi) were then used according to the manufacturer's protocol. Enrichment was validated by staining purified bone marrow monocytes with antibodies against CD115 (BioLegend, clone: AFS98) and Ly6C (BD Bioscience, clone: AL-21).

Skin wounding model

Wounding, preparation of wound tissue, and cell isolation were performed as previously described (67). A total of 3×10^6 RFP⁺ monocytes were adoptively transferred into each previously wounded C57/BL6 recipient via intravenous injection, either 2 or 12 days after injury. Wounds were excised 4 or 14 days after injury. Recovered cells were stained for flow cytometry and cell sorting using CD11b (eBioscience, clone: M1/70), F4/80 (eBioscience, clone: BM8 or AbD Serotec, clone: CI:A3-1), MHC-II (eBioscience, clone: M5/114.15.2), Ly6C (BD, clone: AL-21), CD45 (eBioscience, clone: 30-F11), and CD301b (BioLegend, clone: URA-1). Dead cells were excluded by 4',6-diamidino-2-phenylindole staining (50 ng/ml; Thermo Fisher Scientific).

Flow cytometry

Cells were stained for flow cytometric analysis using TIM4 (BioLegend, clone: F31-5G3), CD45.1 (BioLegend, clone: A20), CD115 (BioLegend, clone: AFS98), and F4/80 (BioLegend, clone: BM8). Detection of intracellular *Retnla* mRNA and RELM α protein (catalog no. 500-P214, PeproTech) was performed using PrimeFlow RNA Assays (Thermo Fisher Scientific) following the manufacturer's instructions. Data from stained cells were collected using LSRFortessa flow cytometers (BD Biosciences) with FACSDiva v.9.0, and data were processed using FlowJo v.10.6. For spectral flow cytometry, cells were stained with specified antibodies (see Supplementary Methods) and collected using a Cytek Aurora (Cytek) spectral flow cytometer at the Sidney Kimmel Comprehensive Cancer Center High Parameter Flow Core. Data were processed using CytoExploreR v.1.1.0 (68), followed by UMAP calculation and fluorescence data scaling with a linear regression model in R v.4.0.0 (69) using Seurat

v.4. Data clustering was performed using the Leiden algorithm (70). Stage assignment was performed manually.

Single-cell sequencing and analysis

Detailed strategy is included in Supplementary Methods. Briefly, scRNA-seq of cells from adipose tissue and lamina propria was performed using a 10x Genomics Chromium Controller. Single cells were processed with GemCode Single Cell Platform using GemCode Gel Beads, Chip, and Library Kits (v2) following the manufacturer's protocol targeting 5000 cells sequenced on HiSeq 3000 (Illumina) with 50,000 reads per cell. scRNA-seq of wounded skin was performed as described previously (71, 72) with Illumina 50-base pair paired-end sequencing on a NovaSeq 6000 aiming for 0.5 mio reads per cell. Samples were demultiplexed and aligned using Cell Ranger (10x Genomics), gsnap v.2018-07-04 (73), and featureCounts v.1.6.2 (74) to genome build GRCm38 release 87. Read count matrices were processed, analyzed, and visualized using Seurat v.4 (38) in R v.4.0.0 (69) and scanpy v.1.8 (32) in Python v.3 (75), complemented by SC-Transform (30), Clustree (76), Harmony (31), BBKNN (33), PAGA (34), Slingshot v.1.6.1 (28), and Monocle v.3 (44) plus visualized with a UMAP (77) as a dimensionality reduction approach. Pathway enrichment and protein interaction network were determined using goseq v.1.40.0 (78), StringDB (79), igraph v.1.2.5 (80), and ggraph v.2.0.2 (81). Network clustering was performed using the cluster_louvain function (82). Trajectory-dependent gene regulation was calculated on top 2000 most variable genes using gam v.1.20 (83). Query datasets available from public repositories were retrieved (table S2), macrophages extracted based on a "Macrophage score" (table S1) and processed as described above. Flow cytometry data associated with individually barcoded cells were used to calculate a UMAP projection using uwot (84), which was then clustered with k-means v.4.0.0 (69), setting k based on the total within cluster sum of squares. TF enrichment analysis was performed with RcisTarget v.1.8.0 (85, 86) and visualized using wordcloud2 v.0.2.1 (87).

Quantification and statistical analysis

Statistical analysis was performed in R v.4.0.0 (69), using functions from the base stats package to calculate a single-factor analysis of variance (ANOVA) with AOV followed by Tukey's honest significant differences to determine statistically significant differences between means (Fig. 2, G and H) with a Bonferroni correction or only a single-factor ANOVA to establish significant clustering effects (Fig. 5M). Tests were two-sided and $\alpha = 0.05$. Ex vivo results are represented as dots for individual mice.

SUPPLEMENTARY MATERIALS

www.science.org/doi/10.1126/sciimmunol.abl7482

Methods

Figs. S1 to S8

Tables S1 to S3

Data files S1 to S3

Materials Design Analysis Reporting (MDAR) Checklist

[View/request a protocol for this paper from Bio-protocol.](#)

REFERENCES AND NOTES

1. Y. Lavin, D. Winter, R. Blecher-Gonen, E. David, H. Keren-Shaul, M. Merad, S. Jung, I. Amit, Tissue-resident macrophage enhancer landscapes are shaped by the local microenvironment. *Cell* **159**, 1312–1326 (2014).
2. E. L. Gautier, T. Shay, J. Miller, M. Greter, C. Jakubczik, S. Ivanov, J. Helft, A. Chow, K. G. Elpek, S. Gordonov, A. R. Mazloom, A. Ma'ayan, W.-J. Chua, T. H. Hansen, S. J. Turley, M. Merad, G. J. Randolph; Immunological Genome Consortium, Gene-expression profiles

- and transcriptional regulatory pathways that underlie the identity and diversity of mouse tissue macrophages. *Nat. Immunol.* **13**, 1118–1128 (2012).
3. T. A. Wynn, A. Chawla, J. W. Pollard, Macrophage biology in development, homeostasis and disease. *Nature* **496**, 445–455 (2013).
 4. G. Hoeffel, F. Ginhoux, Fetal monocytes and the origins of tissue-resident macrophages. *Cell. Immunol.* **330**, 5–15 (2018).
 5. E. Mass, I. Ballesteros, M. Farlik, F. Halbritter, P. Günther, L. Crozet, C. E. Jacome-Galarza, K. Händler, J. Klughammer, Y. Kobayashi, E. Gomez-Perdiguerro, J. L. Schultze, M. Beyer, C. Bock, F. Geissmann, Specification of tissue-resident macrophages during organogenesis. *Science* **353**, eaf4238 (2016).
 6. Z. Liu, Y. Gu, S. Chakarov, C. Blierot, I. Kwok, X. Chen, A. Shin, W. Huang, R. J. Dress, C.-A. Dutertre, A. Schlitzer, J. Chen, L. G. Ng, H. Wang, Z. Liu, B. Su, F. Ginhoux, Fate mapping via Ms4a3-expression history traces monocyte-derived cells. *Cell* **178**, 1509–1525.e19 (2019).
 7. D. Hashimoto, A. Chow, C. Noizat, P. Teo, M. B. Beasley, M. Leboeuf, C. D. Becker, P. See, J. Price, D. Lucas, M. Greter, A. Mortha, S. W. Boyer, E. C. Forsberg, M. Tanaka, N. van Rooijen, A. García-Sastre, E. R. Stanley, F. Ginhoux, P. S. Frenette, M. Merad, Tissue-resident macrophages self-maintain locally throughout adult life with minimal contribution from circulating monocytes. *Immunity* **38**, 792–804 (2013).
 8. C. C. Bain, C. A. Hawley, H. Garner, C. L. Scott, A. Schridde, N. J. Steers, M. Mack, A. Joshi, M. Williams, A. M. I. Mowat, F. Geissmann, S. J. Jenkins, Long-lived self-renewing bone marrow-derived macrophages displace embryo-derived cells to inhabit adult serous cavities. *Nat. Commun.* **7**, ncomms11852 (2016).
 9. C. C. Bain, A. Bravo-Blas, C. L. Scott, E. G. Perdiguerro, F. Geissmann, S. Henri, B. Malissen, L. C. Osborne, D. Artis, A. M. Mowat, Constant replenishment from circulating monocytes maintains the macrophage pool in the intestine of adult mice. *Nat. Immunol.* **15**, 929–937 (2014).
 10. M. Williams, F. R. Svedberg, Does tissue imprinting restrict macrophage plasticity? *Nat. Immunol.* **22**, 118–127 (2021).
 11. Z. Bian, Y. Gong, T. Huang, C. Z. W. Lee, L. Bian, Z. Bai, H. Shi, Y. Zeng, C. Liu, J. He, J. Zhou, X. Li, Z. Li, Y. Ni, C. Ma, L. Cui, R. Zhang, J. K. Y. Chan, L. G. Ng, Y. Lan, F. Ginhoux, B. Liu, Deciphering human macrophage development at single-cell resolution. *Nature* **582**, 571–576 (2020).
 12. L. van de Laar, W. Saelens, S. De Pijck, L. Martens, C. L. Scott, G. Van Isterdael, E. Hoffmann, R. Beyaert, Y. Saeys, B. N. Lambrecht, M. Williams, Yolk sac macrophages, fetal liver, and adult monocytes can colonize an empty niche and develop into functional tissue-resident macrophages. *Immunity* **44**, 755–768 (2016).
 13. C. Blierot, S. Chakarov, F. Ginhoux, Determinants of resident tissue macrophage identity and function. *Immunity* **52**, 957–970 (2020).
 14. P. J. Murray, Macrophage polarization. *Annu. Rev. Physiol.* **79**, 541–566 (2017).
 15. P. J. Murray, J. E. Allen, S. K. Biswas, E. A. Fisher, D. W. Gilroy, S. Goerdt, S. Gordon, J. A. Hamilton, L. B. Ivashkiv, T. Lawrence, M. Locati, A. Mantovani, F. O. Martinez, J.-L. Mege, D. M. Mosser, G. Natoli, J. P. Saeij, J. L. Schultze, K. A. Shirey, A. Sica, J. Suttles, I. Udalova, J. A. van Genderachter, S. N. Vogel, T. A. Wynn, Macrophage activation and polarization: Nomenclature and experimental guidelines. *Immunity* **41**, 14–20 (2014).
 16. D. E. Sanin, M. Matsushita, R. I. Klein Geltink, K. M. Grzes, N. van Teijlingen Bakker, M. Corrado, A. M. Kabat, M. D. Buck, J. Qiu, S. J. Lawless, A. M. Cameron, M. Villa, F. Baixel, A. E. Patterson, F. Hässler, J. D. Curtis, C. M. O'Neill, D. O'Sullivan, D. Wu, G. Mittler, S. C.-C. Huang, E. L. Pearce, E. J. Pearce, Mitochondrial membrane potential regulates nuclear gene expression in macrophages exposed to prostaglandin E2. *Immunity* **49**, 1021–1033.e6 (2018).
 17. J. Xue, S. V. Schmidt, J. Sander, A. Draffehn, W. Krebs, I. Quester, D. De Nardo, T. D. Gohel, M. Emde, L. Schmidleithner, H. Ganesan, A. Nino-Castro, M. R. Mallmann, L. Labzin, H. Theis, M. Kraut, M. Beyer, E. Latz, T. C. Freeman, T. Ulas, J. L. Schultze, Transcriptome-based network analysis reveals a spectrum model of human macrophage activation. *Immunity* **40**, 274–288 (2014).
 18. R. M. Jin, J. Warunek, E. A. Wohlfert, Chronic infection stunts macrophage heterogeneity and disrupts immune-mediated myogenesis. *JCI Insight* **3**, e121549 (2018).
 19. D. Aran, A. P. Looney, L. Liu, E. Wu, Y. Fong, A. Hsu, S. Chak, R. P. Naikawadi, P. J. Wolters, A. R. Abate, A. J. Butte, M. Bhattacharya, Reference-based analysis of lung single-cell sequencing reveals a transitional profibrotic macrophage. *Nat. Immunol.* **20**, 163–172 (2019).
 20. Y. Duan, L. Zeng, C. Zheng, B. Song, F. Li, X. Kong, K. Xu, Inflammatory links between high fat diets and diseases. *Front. Immunol.* **9**, 2649 (2018).
 21. E. Ydens, L. Amann, B. Asselbergh, C. L. Scott, L. Martens, D. Sichien, O. Mossad, T. Blank, S. De Pijck, D. Low, T. Masuda, Y. Saeys, Y. Timmerman, R. Stumm, F. Ginhoux, M. Prinz, S. Janssens, M. Williams, Profiling peripheral nerve macrophages reveals two macrophage subsets with distinct localization, transcriptome and response to injury. *Nat. Neurosci.* **23**, 676–689 (2020).
 22. I. Marigo, R. Trovato, F. Hofer, V. Ingangi, G. Desantis, K. Leone, F. De Sanctis, S. Ugel, S. Canè, A. Simonelli, A. Lamolinara, M. Iezzi, M. Fassan, M. Rugge, F. Boschi, G. Borile, T. Eisenhaure, S. Sarkizova, D. Lieb, N. Hacohen, L. Azzolin, S. Piccolo, R. Lawlor, A. Scarpa, L. Carboognin, E. Bria, S. Bicciato, P. J. Murray, V. Bronte, Disabled homolog 2 controls prometastatic activity of tumor-associated macrophages. *Cancer Discov.* **10**, 1758–1773 (2020).
 23. J.-D. Lin, H. Nishi, J. Poles, X. Niu, C. Mccauley, K. Rahman, E. J. Brown, S. T. Yeung, N. Vozhilla, A. Weinstock, S. A. Ramsey, E. A. Fisher, P. Loke, Single-cell analysis of fate-mapped macrophages reveals heterogeneity, including stem-like properties, during atherosclerosis progression and regression. *JCI Insight* **4**, e124574 (2019).
 24. M. K. Terkelsen, S. M. Bendixen, D. Hansen, E. A. H. Scott, A. F. Moeller, R. Nielsen, S. Mandrup, A. Schlosser, T. L. Andersen, G. L. Sorensen, A. Krag, K. N. Natarajan, S. Detlefsen, H. Dimke, K. Ravnkjaer, Transcriptional dynamics of hepatic sinusoid-associated cells after liver injury. *Hepatology* **72**, 2119–2133 (2020).
 25. S. Xu-Vanpala, M. E. Deerhake, J. D. Wheaton, M. E. Parker, P. R. Juvvadi, N. MacIver, M. Ciofani, M. L. Shinohara, Functional heterogeneity of alveolar macrophage population based on expression of CXCL2. *Sci. Immunol.* **5**, eaba7350 (2020).
 26. K. R. King, A. D. Aguirre, Y.-X. Ye, Y. Sun, J. D. Roh, R. P. Ng Jr., R. H. Kohler, S. P. Arlauckas, Y. Iwamoto, A. Savol, R. I. Sadreyev, M. Kelly, T. P. Fitzgibbons, K. A. Fitzgerald, T. Mitchison, P. Libby, M. Nahrendorf, R. Weissleder, IRF3 and type I interferons fuel a fatal response to myocardial infarction. *Nat. Med.* **23**, 1481–1487 (2017).
 27. K. E. Ronning, S. J. Karlen, E. B. Miller, M. E. Burns, Molecular profiling of resident and infiltrating mononuclear phagocytes during rapid adult retinal degeneration using single-cell RNA sequencing. *Sci. Rep.* **9**, 4858 (2019).
 28. K. Street, D. Risso, R. B. Fletcher, D. Das, J. Ngai, N. Yosef, E. Purdom, S. Dudoit, Slingshot: Cell lineage and pseudotime inference for single-cell transcriptomics. *BMC Genomics* **19**, 477 (2018).
 29. C. Goudot, A. Coillard, A.-C. Villani, P. Gueguen, A. Cros, S. Sarkizova, T.-L. Tang-Huau, M. Bohec, S. Baulande, N. Hacohen, S. Amigorena, E. Segura, Aryl hydrocarbon receptor controls monocyte differentiation into dendritic cells versus macrophages. *Immunity* **47**, 582–596.e6 (2017).
 30. C. Hafemeister, R. Satija, Normalization and variance stabilization of single-cell RNA-seq data using regularized negative binomial regression. *Genome Biol.* **20**, 296 (2019).
 31. I. Korsunsky, N. Millard, J. Fan, K. Slowikowski, F. Zhang, K. Wei, Y. Baglaenko, M. Brenner, P.-R. Loh, S. Raychaudhuri, Fast, sensitive and accurate integration of single-cell data with Harmony. *Nat. Methods* **16**, 1289–1296 (2019).
 32. F. A. Wolf, P. Angerer, F. J. Theis, SCANPY: Large-scale single-cell gene expression data analysis. *Genome Biol.* **19**, 15 (2018).
 33. K. Polański, M. D. Young, Z. Miao, K. B. Meyer, S. A. Teichmann, J.-E. Park, BBKNN: Fast batch alignment of single cell transcriptomes. *Bioinformatics* **36**, 964–965 (2020).
 34. F. A. Wolf, F. K. Hamey, M. Plass, J. Solana, J. S. Dahlin, B. Göttgens, N. Rajewsky, L. Simon, F. J. Theis, PAGA: Graph abstraction reconciles clustering with trajectory inference through a topology preserving map of single cells. *Genome Biol.* **20**, 59 (2019).
 35. T. Liu, H. Yu, M. Ullenbruch, H. Jin, T. Ito, Z. Wu, J. Liu, S. H. Phan, The in vivo fibrotic role of FIZZ1 in pulmonary fibrosis. *PLOS ONE* **9**, e88362 (2014).
 36. J. Li, S. Y. Kim, N. M. Lainez, D. Coss, M. G. Nair, Macrophage-regulatory T cell interactions promote type 2 immune homeostasis through resistin-like molecule α . *Front. Immunol.* **12**, 710406 (2021).
 37. B. Krljanac, C. Schubart, R. Naumann, S. Wirtz, S. Culemann, G. Krönke, D. Voehringer, RELMa-expressing macrophages protect against fatal lung damage and reduce parasite burden during helminth infection. *Sci. Immunol.* **4**, eaau3814 (2019).
 38. T. Stuart, A. Butler, P. Hoffman, C. Hafemeister, E. Papalexi, W. M. Mauck III, Y. Hao, M. Stoeckius, P. Smibert, R. Satija, Comprehensive integration of single-cell data. *Cell* **177**, 1888–1902.e21 (2019).
 39. Q. Huang, Y. Liu, Y. Du, L. X. Garmire, Evaluation of cell type annotation R packages on single-cell RNA-seq data. *Genom. Proteom. Bioinform.* **19**, 267–281 (2021).
 40. M. D. Luecken, M. Büttner, K. Chaichoompu, A. Danese, M. Interlandi, M. F. Mueller, D. C. Strobl, L. Zappia, M. Dugas, M. Colomé-Tatché, F. J. Theis, Benchmarking atlas-level data integration in single-cell genomics. *Nat. Methods* **19**, 41–50 (2020).
 41. Y. Fujiyama, R. Hokari, S. Miura, C. Watanabe, S. Komoto, T. Oyama, C. Kurihara, H. Nagata, T. Hibi, Butter feeding enhances TNF- α production from macrophages and lymphocyte adherence in murine small intestinal microvessels. *J. Gastroenterol. Hepatol.* **22**, 1838–1845 (2007).
 42. T. R. Hammond, C. Dufort, L. Dissing-Olesen, S. Giera, A. Young, A. Wysoker, A. J. Walker, F. Gergits, M. Segel, J. Nemesh, S. E. Marsh, A. Saunders, E. Macosko, F. Ginhoux, J. Chen, R. J. M. Franklin, X. Piao, S. A. McCarroll, B. Stevens, Single-cell RNA sequencing of microglia throughout the mouse lifespan and in the injured brain reveals complex cell-state changes. *Immunity* **50**, 253–271.e6 (2019).
 43. S. A. Eming, T. A. Wynn, P. Martin, Inflammation and metabolism in tissue repair and regeneration. *Science* **356**, 1026–1030 (2017).
 44. C. Trapnell, D. Cacchiarelli, J. Grimsby, P. Pokharel, S. Li, M. Morse, N. J. Lennon, K. J. Livak, T. S. Mikkelsen, J. L. Rinn, The dynamics and regulators of cell fate decisions are revealed by pseudotemporal ordering of single cells. *Nat. Biotechnol.* **32**, 381–386 (2014).
 45. J. S. Seidman, T. D. Troutman, M. Sakai, A. Gola, N. J. Spann, H. Bennett, C. M. Bruni, Z. Ouyang, R. Z. Li, X. Sun, B. T. Vu, M. P. Pasillas, K. M. Ego, D. Gosselin, V. M. Link,

- L-W. Chong, R. M. Evans, B. M. Thompson, J. G. McDonald, M. Hosseini, J. L. Witztum, R. N. Germain, C. K. Glass, Niche-specific reprogramming of epigenetic landscapes drives myeloid cell diversity in nonalcoholic steatohepatitis. *Immunity* **52**, 1057–1074.e7 (2020).
46. C. Bain, C. L. Scott, H. Uronen-Hansson, S. Gudjonsson, O. Jansson, O. Grip, M. Williams, B. Malissen, W. W. Agace, A. M. Mowat, Resident and pro-inflammatory macrophages in the colon represent alternative context-dependent fates of the same Ly6Chi monocyte precursors. *Mucosal Immunol.* **6**, 498–510 (2013).
 47. S. Culemann, A. Grüneboom, J. Á. Nicolás-Ávila, D. Weidner, K. F. Lämmle, T. Rothe, J. A. Quintana, P. Kirchner, B. Krljanac, M. Eberhardt, F. Ferrazzi, E. Kretzschmar, M. Schicht, K. Fischer, K. Gelse, M. Faas, R. Pfeifle, J. A. Ackermann, M. Pachowsky, N. Renner, F. Simon, R. F. Haseloff, A. B. Ekici, T. Bäuerle, I. E. Blasig, J. Vera, D. Voehringer, A. Kleyer, F. Paulsen, G. Schett, A. Hidalgo, G. Krönke, Locally renewing resident synovial macrophages provide a protective barrier for the joint. *Nature* **572**, 670–675 (2019).
 48. E. Sajti, V. M. Link, Z. Ouyang, N. J. Spann, E. Westin, C. E. Romanoski, G. J. Fonseca, L. S. Prince, C. K. Glass, Transcriptomic and epigenetic mechanisms underlying myeloid diversity in the lung. *Nat. Immunol.* **21**, 221–231 (2020).
 49. L. Huang, E. V. Nazarova, S. Tan, Y. Liu, D. G. Russell, Growth of Mycobacterium tuberculosis in vivo segregates with host macrophage metabolism and ontogeny. *J. Exp. Med.* **215**, 1135–1152 (2018).
 50. F. R. Svedberg, S. L. Brown, M. Z. Krauss, L. Campbell, C. Sharpe, M. Clausen, G. J. Howell, H. Clark, J. Madsen, C. M. Evans, T. E. Sutherland, A. C. Ivens, D. J. Thornton, R. K. Grencis, T. Hussell, D. M. Cunoosamy, P. C. Cook, A. S. MacDonald, The lung environment controls alveolar macrophage metabolism and responsiveness in type 2 inflammation. *Nat. Immunol.* **20**, 571–580 (2019).
 51. U. M. Gundra, N. M. Giris, D. Ruckerl, S. Jenkins, L. N. Ward, Z. D. Kurtz, K. E. Wiens, M. S. Tang, U. Basu-Roy, A. Mansukhani, J. E. Allen, P. Loke, Alternatively activated macrophages derived from monocytes and tissue macrophages are phenotypically and functionally distinct. *Blood* **123**, e110–e122 (2014).
 52. S. J. Jenkins, D. Ruckerl, P. C. Cook, L. H. Jones, F. D. Finkelman, N. van Rooijen, A. S. MacDonald, J. E. Allen, Local macrophage proliferation, rather than recruitment from the blood, is a signature of TH2 inflammation. *Science* **332**, 1284–1288 (2011).
 53. B.-Z. Qian, J. Li, H. Zhang, T. Kitamura, J. Zhang, L. R. Campion, E. A. Kaiser, L. A. Snyder, J. W. Pollard, CCL2 recruits inflammatory monocytes to facilitate breast-tumour metastasis. *Nature* **475**, 222–225 (2011).
 54. Y.-T. Wang, K. Zaitsev, Q. Lu, S. Li, W. T. Schaff, K.-W. Kim, L. Droit, C. B. Wilen, C. Desai, D. R. Balce, R. C. Orchard, A. Orvedahl, S. Park, D. Kreamealmeyer, S. A. Handley, J. D. Pfeiffer, M. T. Baldrige, M. N. Artyomov, C. L. Stallings, H. W. Virgin, Select autophagy genes maintain quiescence of tissue-resident macrophages and increase susceptibility to Listeria monocytogenes. *Nat. Microbiol.* **5**, 272–281 (2020).
 55. H. Aegerter, J. Kulikaukaitė, S. Crotta, H. Patel, K. Kelly, E. M. Hessel, M. Mack, S. Beinke, A. Wack, Influenza-induced monocyte-derived alveolar macrophages confer prolonged antibacterial protection. *Nat. Immunol.* **21**, 145–157 (2020).
 56. N. A-Gonzalez, J. A. Quintana, S. García-Silva, M. Mazariegos, A. González de la Aleja, J. A. Nicolás-Ávila, W. Walter, J. M. Adrover, G. Crainiciuc, V. K. Kuchroo, C. V. Rothlin, H. Peinado, A. Castrillo, M. Ricote, A. Hidalgo, Phagocytosis imprints heterogeneity in tissue-resident macrophages. *J. Exp. Med.* **214**, 1281–1296 (2017).
 57. M. H. Askenase, B. A. Goods, H. E. Beatty, A. F. Steinschneider, S. E. Velazquez, A. Osheroov, M. J. Landreneau, S. L. Carroll, T. B. Tran, V. S. Avram, R. S. Drake, G. J. Gatter, J. A. Massey, S. S. Karuppagounder, R. R. Ratan, C. C. Matouk, K. N. Sheth, W. C. Ziai, A. R. Parry-Jones, I. A. Awad, M. Zuccarello, R. E. Thompson, J. Dawson, D. F. Hanley, J. C. Love, A. K. Shalek, L. H. Sansing; MISTIE III Consortium; ICHseq investigators; ICHseq Investigators MISTIE III Investigators, Longitudinal transcriptomics define the stages of myeloid activation in the living human brain after intracerebral hemorrhage. *Sci. Immunol.* **6**, eabd6279 (2021).
 58. C. M. Minutti, L. H. Jackson-Jones, B. García-Fojeda, J. A. Knipper, T. E. Sutherland, N. Logan, E. Ringqvist, R. Guilleamat-Prats, D. A. Ferenbach, A. Artigas, C. Stamme, Z. C. Chronos, D. M. Zaiss, C. Casals, J. E. Allen, Local amplifiers of IL-4R α -mediated macrophage activation promote repair in lung and liver. *Science* **356**, 1076–1080 (2017).
 59. L. Bosurgi, Y. G. Cao, M. Cabeza-Cabrerizo, A. Tucci, L. D. Hughes, Y. Kong, J. S. Weinstein, P. Licona-Limon, E. T. Schmid, F. Pelorosso, N. Gagliani, J. E. Craft, R. A. Flavell, S. Ghosh, C. V. Rothlin, Macrophage function in tissue repair and remodeling requires IL-4 or IL-13 with apoptotic cells. *Science* **356**, 1072–1076 (2017).
 60. T. Liu, B. Zhu, Y. Liu, X. Zhang, J. Yin, X. Li, L. Jiang, A. P. Hodges, S. B. Rosenthal, L. Zhou, J. Yancey, A. McQuade, M. Blurton-Jones, R. E. Tanzi, T. Y. Huang, H. Xu, Multi-omic comparison of Alzheimer's variants in human ESC-derived microglia reveals convergence at APOE. *J. Exp. Med.* **217**, e20200474 (2020).
 61. S. Nakae, L. H. Ho, M. Yu, R. Monteforte, M. Iikura, H. Suto, S. J. Galli, Mast cell-derived TNF contributes to airway hyperreactivity, inflammation, and TH2 cytokine production in an asthma model in mice. *J. Allergy Clin. Immunol.* **120**, 48–55 (2007).
 62. S. J. Galli, N. Gaudenzio, M. Tsai, Mast cells in inflammation and disease: Recent progress and ongoing concerns. *Annu. Rev. Immunol.* **38**, 49–77 (2020).
 63. D. R. Herbert, B. Douglas, K. Zullo, Group 2 innate lymphoid cells (ILC2): Type 2 immunity and helminth immunity. *Int. J. Mol. Sci.* **20**, 2276 (2019).
 64. D. G. Ryan, M. P. Murphy, C. Frezza, H. A. Prag, E. T. Chouchani, L. A. O'Neill, E. L. Mills, Coupling Krebs cycle metabolites to signalling in immunity and cancer. *Nat. Metab.* **1**, 16–33 (2019).
 65. D. R. Herbert, C. Hölscher, M. Mohrs, B. Arendse, A. Schwegmann, M. Radwanska, M. Leeto, R. Kirsch, P. Hall, H. Mossmann, B. Claussen, I. Förster, F. Brombacher, Alternative macrophage activation is essential for survival during schistosomiasis and downmodulates T helper 1 responses and immunopathology. *Immunity* **20**, 623–635 (2004).
 66. H. Luche, O. Weber, T. Nageswara Rao, C. Blum, H. J. Fehling, Faithful activation of an extra-bright red fluorescent protein in “knock-in” Cre-reporter mice ideally suited for lineage tracing studies. *Eur. J. Immunol.* **37**, 43–53 (2007).
 67. S. Willenborg, B. Eckes, J. Brinckmann, T. Krieg, A. Waisman, K. Hartmann, A. Roers, S. A. Eming, Genetic ablation of mast cells redefines the role of mast cells in skin wound healing and bleomycin-induced fibrosis. *J. Invest. Dermatol.* **134**, 2005–2015 (2014).
 68. D. Hammill, CytoExploreR: Interactive Analysis of Cytometry Data (2021); <https://github.com/DillonHammill/CytoExploreR>.
 69. R Core Team, R: A Language and Environment for Statistical Computing (2013); www.R-project.org/.
 70. V. A. Traag, L. Waltman, N. J. van Eck, From Louvain to Leiden: Guaranteeing well-connected communities. *Sci. Rep.* **9**, 5233 (2019).
 71. S. Picelli, O. R. Faridani, A. K. Björklund, G. Winberg, S. Sagasser, R. Sandberg, Full-length RNA-seq from single cells using Smart-seq2. *Nat. Protoc.* **9**, 171–181 (2014).
 72. S. Willenborg, D. E. Sanin, A. Jais, X. Ding, T. Ulas, J. Nüchel, M. Popović, T. MacVicar, T. Langer, J. L. Schultze, A. Gerbaulet, A. Roers, E. J. Pearce, J. C. Brüning, A. Trifunovic, S. A. Eming, Mitochondrial metabolism coordinates stage-specific repair processes in macrophages during wound healing. *Cell Metab.* **33**, 2398–2414.e9 (2021).
 73. T. D. Wu, S. Nacu, Fast and SNP-tolerant detection of complex variants and splicing in short reads. *Bioinformatics* **26**, 873–881 (2010).
 74. Y. Liao, G. K. Smyth, W. Shi, The R package Rsubread is easier, faster, cheaper and better for alignment and quantification of RNA sequencing reads. *Nucleic Acids Res.* **47**, e47 (2019).
 75. G. Van Rossum, F. L. Drake, *Python 3 Reference Manual: (Python Documentation Manual Part 2)* (CreateSpace Independent Publishing Platform, 2009); <https://play.google.com/store/books/details?id=KlybQQAACAAJ>.
 76. L. Zappia, A. Oshlack, Clustering trees: A visualization for evaluating clusterings at multiple resolutions. *Gigascience* **7**, gij083 (2018).
 77. L. McInnes, J. Healy, N. Saul, L. Großberger, UMAP: Uniform Manifold Approximation and Projection. *J. Open Source Softw.* **3**, 861 (2018).
 78. M. D. Young, M. J. Wakefield, G. K. Smyth, A. Oshlack, Gene ontology analysis for RNA-seq: Accounting for selection bias. *Genome Biol.* **11**, R14 (2010).
 79. D. Szklarczyk, A. L. Gable, D. Lyon, A. Junge, S. Wyder, J. Huerta-Cepas, M. Simonovic, N. T. Doncheva, J. H. Morris, P. Bork, L. J. Jensen, C. von Mering, STRING v11: Protein-protein association networks with increased coverage, supporting functional discovery in genome-wide experimental datasets. *Nucleic Acids Res.* **47**, D607–D613 (2019).
 80. G. Csardi, T. Nepusz, The igraph software package for complex network research. *InterJournal. Complex Syst.* **1695**, 1–9 (2006).
 81. T. L. Pedersen, ggraph: An Implementation of Grammar of Graphics for Graphs and Networks (2020); <https://CRAN.R-project.org/package=ggraph>.
 82. V. D. Blondel, J.-L. Guillaume, R. Lambiotte, E. Lefebvre, Fast unfolding of communities in large networks. *J. Stat. Mech.* **2008**, P10008 (2008).
 83. T. Hastie, gam: Generalized Additive Models (2020); <https://CRAN.R-project.org/package=gam>.
 84. J. Melville, uwot: The Uniform Manifold Approximation and Projection (UMAP) Method for Dimensionality Reduction (2020); <https://CRAN.R-project.org/package=uwot>.
 85. S. Aibar, C. B. Gonzalez-Blas, T. Moerman, V. A. Huynh-Thu, H. Imrichova, G. Hulselms, F. Rambow, J.-C. Marine, P. Geurts, J. Aerts, J. van den Oord, Z. Kalender Atak, J. Wouters, S. Aerts, SCENIC: Single-cell regulatory network inference and clustering. *Nat. Methods* **14**, 1083–1086 (2017).
 86. S. Aibar, S. Aerts, RcisTarget. *Bioconductor* (2016); <https://bioconductor.org/packages/release/bioc/html/RcisTarget.html>.
 87. D. Lang, G.-T. Chien, wordcloud2: Create Word Cloud by “htmlwidget” (2018); <https://CRAN.R-project.org/package=wordcloud2>.

Acknowledgments: We would like to thank M. Nair and J. Li at University of California Riverside for providing RELMu-deficient monocytes to conduct our study. We would also like to acknowledge P. Gueguen, B. Kelly, members of the Pearce laboratories, the staff at the DeepSequencing and Bioinformatics facilities at the MPI-IE, as well as the members of the single-cell unit from the DRESDEN-concept Genome Center for technical support and constructive criticism. **Funding:** This study was supported by the NIH (AI110481 to E.J.P.), the

Max Planck Society, and the German Research Foundation (Leibniz Prize to E.L.P.; Germany's Excellence Strategy: CIBSS EXC-2189 Project ID 390939984 to E.L.P. and CECAD EXC-2030 project ID 390661388 to S.A.E.; Research Unit FOR2599 to S.A.E., A.D., A.R., P.J.M., and E.J.P.; and Collaborative Research centers: CRC1218 project ID 269925409 and CRC1403 project ID 1403-414786233 to S.A.E.). A.M.K., A.C., and S.D. were supported by the Alexander von Humboldt Fellowship Foundation. **Author contributions:** Conceptualization: D.E.S., S.A.E., A.G., A.R., P.J.M., and E.J.P. Methodology: D.E.S. Software: D.E.S. Formal analysis: D.E.S. Investigation: D.E.S., Y.G., E.M., A.M.K., K.M.G., A.C., G.C., E.A.T., A.G., A.D., S.W., S.R., and J.D.C. Data curation: D.E.S. and Y.G. Writing—original draft: D.E.S. and E.J.P. Writing—review and editing: D.E.S., S.W., S.D., E.L.P., S.A.E., A.G., A.R., P.J.M., and E.J.P. Funding acquisition: E.L.P., S.A.E., A.G., A.R., P.J.M., and E.J.P. Visualization: D.E.S. Supervision: E.J.P. **Competing interests:** E.L.P. and E.J.P. are founders of Rheos Medicines. E.L.P. is an SAB member of ImmunoMet Therapeutics. G.C. is an editor at *Nature*. The other authors declare that they have no competing interests. **Data and materials availability:** An interactive shiny application to visualize critical aspects of the data in this publication can be accessed at <https://tjh.edu/>

macrophage-framework. scRNA-seq datasets generated specifically for this publication may be retrieved from publicly available repositories with no restrictions on their use, under the following accession numbers: helminth infection of adipose tissue (GSE157313), bacterial infection of adipose tissue (GSE171328), HFD lamina propria (GSE171330), and skin wound (GSE183489). Accession numbers, associated publications, and experimental details of these and all other datasets included in this study are listed in table S2. Annotated code to reproduce key analysis modules and recreate figures was deposited on GitHub and may be accessed at https://github.com/davidsanin/Macrophage_framework. All other data needed to evaluate the conclusions in the paper are present in the paper or the Supplementary Materials.

Submitted 3 August 2021
Resubmitted 21 December 2021
Accepted 16 March 2022
Published 15 April 2022
10.1126/sciimmunol.abl7482

A common framework of monocyte-derived macrophage activation

David E. SaninYan GeEmilija MarinkovicAgnieszka M. KabatAngela CastoldiGeorge CaputaKatarzyna M. GrzesJonathan D. CurtisElizabeth A. ThompsonSebastian WillenborgStefanie DichtlSusanne ReinhardtAndreas DahlErika L. PearceSabine A. EmingAlexander GerbauletAxel RoersPeter J. MurrayEdward J. Pearce

Sci. Immunol., 7 (70), eabl7482. • DOI: 10.1126/sciimmunol.abl7482

A macrophage classification system

Monocytes infiltrating tissues in response to infection or inflammation rapidly differentiate into macrophages that can display a wide range of activation states. Using single-cell transcriptomics, Sanin *et al.* develop a framework for classifying macrophage activation states across different tissues and stimuli. On the basis of analysis of adipose tissue macrophages collected from mice infected with *Listeria monocytogenes* or the helminth *Heligmosomoides polygyrus*, the authors defined four activation paths including “phagocytic,” “inflammatory,” “oxidative stress,” and “remodeling” paths. Transient RELM β expression occurring independently of IL-4 signaling was a conserved feature of all early-infiltrating macrophages. This predictive framework was validated using a large-scale, integrated analysis of published transcriptomic data, highlighting that specific features of macrophage activation are conserved across a wide range of tissues and disease states (see the related Focus commentary by Loke *et al.*).

View the article online

<https://www.science.org/doi/10.1126/sciimmunol.abl7482>

Permissions

<https://www.science.org/help/reprints-and-permissions>

Use of this article is subject to the [Terms of service](#)

Science Immunology (ISSN) is published by the American Association for the Advancement of Science. 1200 New York Avenue NW, Washington, DC 20005. The title *Science Immunology* is a registered trademark of AAAS.

Copyright © 2022 The Authors, some rights reserved; exclusive licensee American Association for the Advancement of Science. No claim to original U.S. Government Works